A Finite Volume Algorithm for the Two-Fluid Plasma System in One Dimension

John Loverich

A thesis submitted in partial fulfillment of
the requirements for the degree of

Master of Science in Aeronautics and Astronautics

University of Washington

2003

Program Authorized to Offer Degree: Aeronautics and Astronautics

University of Washington

Graduate School

This is to certify that I have examined this copy of a master's thesis by

John Loverich

and have found that it is complete and satisfactory in all respects,
and that any and all revisions required by the final
examining committee have been made.

Committee Members:

_____

Uri Shumlak

_____

Scott Eberhardt

Date: _____

University of Washington

Abstract

A Finite Volume Algorithm for the Two-Fluid Plasma System in One Dimension

by John Loverich

Chair of Supervisory Committee:

Professor Uri Shumlak
Aeronautics and Astronautics

In this thesis an algorithm is developed to numerically solve the two-fluid plasma system in one dimension. The two-fluid plasma system consists of electron and ion continuity equations, electron and ion momentum equations and electron and ion energy equations. The full Maxwell's equations are solved including displacement current and electron and ion currents. The fluids are assumed to be non-relativistic and collisionless. The fluids are coupled to the electromagnetic field through the Lorentz forces. The homogeneous part of the fluid equations and Maxwell's equations are solved numerically using a Roe approximate Riemann solver while the source terms are updated either implicitly or explicitly. The algorithm is tested on several model problems including an electromagnetic shock problem for which it is compared against the MHD solution, an electrostatic shock, and a Debye shielding problem. It is shown that the algorithm is able to accurately resolve various plasma waves including electron plasma waves, R-mode, L-mode, and whistler mode waves.

TABLE OF CONTENTS

LIST OF FIGURES

ACKNOWLEDGMENTS

I received major help on this research from Uri Shumlak who is my adviser and the principal investigator of this project. Chris Aberle, another graduate student, participated in the other half of this project, developing a 3-D Maxwell solver for the two-fluid system. He has been very helpful as a trouble shooter and programming adviser. Travis Burton supplied comic relief by pulling such stunts as nearly cutting off his foot with a grinder while grinding barefoot. Other influential lab characters include Ammar Hakim, David Osburn, Bogdan Udrea, Stuart Jackson and the janitor.

Chapter 1

INTRODUCTION

Many plasma fluid equations describing ion-electron plasmas are reductions of the two-fluid plasma model. Ideal MHD (Magnetohydrodynamics) assumes massless electrons and quasi-neutrality between the electron fluid and the ion fluid. It ignores terms such as the hall term, diamagnetic drift, electron convective terms, and displacement current. The ideal MHD model can be improved with the Hall MHD model by including the Hall term in the Ideal MHD Ohm's law. The term Hall MHD or sometimes two-fluid MHD [6] refers to ideal MHD with the Hall current and sometimes the diamagnetic drift added to Ohm's law, but the electron convective derivative is still ignored. At the other end of the spectrum of fluid models is EMHD or Electron MHD. In EMHD the low frequency ion effects are ignored and only the fast waves are considered. Displacement current, and electron inertia are important effects in EMHD. Finally, another plasma regime corresponds to that of small scale effects and low density plasmas where charge separation is important, in this case quasi-neutrality is not an accurate assumption. The full two-fluid equations encompass all regimes and include the the displacement current and electron convective derivative and a separate electron continuity and energy equations.

The Ideal MHD system is computationally simple to solve and has been studied extensively including certain non-ideal terms such as resistivity and viscosity [29, 15, 1, 2, 7, 30, 10, 31]. The system is hyperbolic and the shortest important time scale is on the order of the Alfven time. Numerical solutions to the more complete Hall MHD system have been driven by the geophysics [22, 13, 6] and fusion [21] community and the desire to understand magnetic reconnection and other effects beyond MHD. The space propulsion community is also interested in more complete models as evidenced by work on the Hall and MPD

thrusters [8, 24]. Work on non-MHD type fluid plasmas have been performed to help understand weakly ionized gas flow [5] and low density non-neutral plasmas [25]. Research has increasingly pushed to more complete fluid plasma models.

Ideal MHD has a limited range of applicability although simple to solve. Hall MHD is more difficult to solve because the whistler wave is resolved numerically. When electron inertia and displacement current are ignored the maximum whistler wave velocity increases with grid resolution in such a way that increasing the resolution of a simulation increases the stiffness of the problem [6]. These problems can be alleviated by introducing displacement current which limits the whistler wave velocity to the speed of light or introducing electron inertia which creates a cutoff for the whistler wave which effectively limits the maximum speed of the whistler wave [22]. In addition, electron inertia is partly responsible for magnetic reconnection [4] and so including electron inertia may allow this phenomena to be modeled. In the two-fluid model these two terms are included in addition to the rest of the electron convective derivative and simplify the numerical solution to certain types of fluid plasma problems. In the two-fluid plasma equations, separate ion and electron continuity equations are used so that quasi-neutrality is not assumed. This allows non-neutral effects such as electron plasma waves and Debye shielding to be modeled. By moving two a two-fluid model fluid plasma regimes spanned by ideal MHD, Hall MHD, EMHD and low density plasmas can be solved with a single algorithm in addition to many effects which cannot be described using any of these simpler models. This type of algorithm will be particularly applicable to fast processes such as z-pinches [26].

The algorithm has been developed with an eye on eventually creating a three dimensional two-fluid algorithm that works on arbitrary geometries. The finite volume method is particularly suited to this problem. Finite volume methods are common in the computational fluid dynamics community [19, 16, 28, 14, 3] and have been developed for electromagnetics [20]. In some regards the two-fluid model is numerically simpler to model than Hall MHD because the whistler wave has a maximum velocity which is independent of grid resolution. However, the tradeoff is that the plasma frequency and the speed of light must be resolved. The system can be written as a balance law with a hyperbolic part set equal to source terms. In the ideal two-fluid system the source terms do not have any derivatives in them

which means that if one wishes to solve the source terms implicitly a local matrix inversion on a finite volume grid is all that is required. In contrast, in Hall MHD, a semi-implicit treatment requires the solution of a global matrix which can be very time consuming [6].

In the first part of this thesis the two-fluid system of equations is introduced and a non-dimensionalization in terms of important plasma parameters is developed. Next, a derivation of the MHD equations from the non-dimensionalization of the two-fluid equations is presented so that the approximations in the MHD equations are apparent. Two-fluid plasma waves are also discussed in terms of their high and low frequency limits. The numerical algorithm is then presented and the conditions for the stability of the algorithm. The results of various simulations are presented and compared to analytic solutions or to published numerical solutions. Finally, the conclusions are discussed in the last chapter.

Chapter 2

THE TWO-FLUID PLASMA SYSTEM

The equations for the two-fluid plasma system consists of two sets of fluid equations and the full Maxwell's equations. The fluid equations differ slightly from the traditional Euler equations because the Lorentz force is added as a source term. The two fluids are the electron fluid and the ion fluid which are both charged fluids. Each fluid is characterized by its own continuity, momentum and energy equations. Maxwell's equations have a source term which is the sum of the electron and ion currents. In addition to the fluid characteristics, ion/electron bulk velocity and ion/electron bulk velocity $\pm$ the speed of sound and the Maxwell characteristics $\pm$ the speed of light, the two-fluid system admits a continuous range of linear waves. It is the purpose of this section to present the two-fluid system of equations and then proceed to identify a non-dimensionalization and then take a look at the large number of simplifications that lead to the much simpler and widely used MHD approximation. A section on two-fluid plasma waves is also included. It is hoped that this analysis will help the reader gain some appreciation for the wide variety of physics that the two-fluid system admits and that the MHD system does not.

2.1 Assumptions

The two-fluid system of equations used in this thesis assumes the electrons are in thermal equilibrium, the ions are in thermal equilibrium and an accurate representation of the currents effecting the electromagnetic fields can be obtained by assuming a Maxwellian distribution of particle velocities. There must be enough particles to make the Maxwellian distribution an accurate representation of the particle distribution function. There are no collisions between particles so there is no viscosity, thermal conduction or resistivity. Debye length is the distance at which the electric field from a point charge is shielded out. Scales smaller than the Debye length can be resolved provided the conditions just discussed are

assumed.

2.2 The Two-Fluid Plasma Equations

In the following the subscript α will denote species and other Greek subscripts and superscripts will represent Cartesian tensor elements. Important variables are,

- m_α = mass of species α,
- q_α = charge of species α,
- n_α = number density of species α,
- ρ_α = mass density of species α,
- P_α = pressure of species α,
- e_α = energy of species α,
- $U_{\beta\alpha}$ = fluid velocity in direction β of species α,
- E_β = electric field in direction β,
- B_β = magnetic field in direction β,
- c = speed of light,
- ϵ_0 = permittivity of free space.

$\epsilon^{\gamma\,\beta\,\nu}$ is the Levi-Cevita tensor which in this case is simply.

$$\epsilon^{\gamma\,\beta\,\nu} = \begin{cases} 0 & \text{when two or more of the superscripts are the same;} \\ 1 & \text{when } \gamma\ \beta\ \nu \text{ are an even permutation of 1,2,3;} \\ -1 & \text{when } \gamma\ \beta\ \nu \text{ are an odd permutation of 1,2,3.} \end{cases} \tag{2.1}$$

The two-fluid equations with source terms are the following,

- **species continuity**

$$\partial_t \left(\rho_\alpha\right) + \nabla_\beta \left(\rho_\alpha U_\alpha^\beta\right) = 0\,, \tag{2.2}$$

- **species momentum**

$$\partial_t \left(\rho_\alpha U^\nu\right) + \nabla_\beta \left(\rho_\alpha U_\alpha^\beta U_\alpha^\nu + \delta^{\beta\nu} P_\alpha\right) = n_\alpha q_\alpha \left(E^\nu + \epsilon^{\nu\,\beta\,\gamma} U_\beta B_\gamma\right)\,, \tag{2.3}$$

- **species energy**

$$\partial_t \left(e_\alpha\right) + \nabla_\beta \left(U_\alpha^\beta\, e_\alpha + U_\alpha^\beta\, P_\alpha\right) = n_\alpha q_\alpha E_\beta U_\alpha^\beta\,, \tag{2.4}$$

- **Ampere's law**

$$\partial_t E^\nu - c^2 \nabla_\beta\, \epsilon^{\nu\,\beta\,\gamma} B_\gamma = -\frac{1}{\epsilon_0} \sum_\alpha n_\alpha q_\alpha U_\alpha^\nu\,, \tag{2.5}$$

- **Faraday's law**

$$\partial_t B^\nu + \nabla_\beta\, \epsilon^{\nu\,\beta\,\gamma} E_\gamma = 0\,, \tag{2.6}$$

- **Poisson's equation**

$$\nabla_\beta E^\beta = \frac{1}{\epsilon_0} \sum_\alpha q_\alpha\, n_\alpha\,, \tag{2.7}$$

- **Magnetic flux condition**

$$\nabla_\beta B^\beta = 0\,. \tag{2.8}$$

When (2.6) and (2.5) are solved exactly, (2.7) and (2.8) are satisfied automatically. However, when the system is discretized errors in (2.7) and (2.8) appear.

In one dimension (2.8) is satisfied exactly because there is no change in the B field in the x direction. This issue will be addressed when the solver is extended to 3 dimensions. The technique of Munz [20] is used in order to satisfy (2.7). Maxwell's equations are re-written to include a correction potential, ϕ, which propagates the error in (2.7) out of the domain at the speed Γ. To accommodate the new variable, (2.6) and (2.7) are altered as follows,

- **Modified Ampere's law**

$$\partial_t E^\nu - c^2 \nabla_\beta \left(\epsilon^{\nu\,\beta\,\gamma} B_\gamma + \delta^{\nu\,\beta} \phi\right) = -\frac{1}{\epsilon_0} \sum_\alpha n_\alpha q_\alpha U_\alpha^\nu\,, \tag{2.9}$$

- **Modified Poisson's equation**

$$\partial_t \phi + \Gamma^2 \nabla_\beta E^\beta = \frac{\Gamma^2}{\epsilon_0} \sum_\alpha q_\alpha \, n_\alpha \, . \tag{2.10}$$

In all cases it will be indicated whether the modified or unmodified equations are used.

2.3 Non-Dimensionalization

The two-fluid system describes fluid behavior over several different regimes including the MHD regime where the electron fluid and ion fluid are tightly bound through electromagnetic fields and a decoupled regime where the coupling between fluids is so weak that the fluids move independently. These different regimes are simple to describe. Several non-dimensional factors are developed that are composed of common plasma variables; these variables characterize the regime. The non-dimensional barred variables are defined as follows

- $\bar{x} = \frac{x}{x_0}$,
- $\bar{n}_\alpha = \frac{n_\alpha}{n_0}$,
- $\bar{q} = \frac{q}{q_0}$,
- $\bar{m}_\alpha = \frac{m_\alpha}{m_i}$,
- $\bar{U}_{\beta\,\alpha} = \frac{U_{\beta\,\alpha}}{U_0}$,
- $\bar{P}_\alpha = \frac{P_\alpha}{m_i \, n_0 \, U_0^2}$,
- $\bar{e}_\alpha = \frac{e_\alpha}{m_i \, n_0 \, U_0^2}$,
- $\bar{t} = \frac{t}{t_0}$,
- $\bar{E}_\beta = \frac{E_\beta}{E_0}$,

- $\bar{B}_\beta = \frac{B_\beta}{B_0}$,
- $\bar{c} = \frac{c}{U_0}$.

The dimensional variables of the previous section are re-written in terms of these non-dimensional variables as,

- **Non-dimensional form of species continuity** (2.2)

$$\partial_{\bar{t}}\left(\bar{\rho}_\alpha\right) + F\ \bar{\nabla}_\beta\left(\bar{\rho}_\alpha \bar{U}_\alpha^\beta\right) = 0\,, \tag{2.11}$$

with

$$F\ = \frac{U_0\, t_0}{x_0}\,, \tag{2.12}$$

- **Non-dimensional form of species momentum** (2.3)

$$\partial_{\bar{t}}\left(\bar{\rho}_\alpha \bar{U}_\alpha^\nu\right) + F\ \bar{\nabla}_\beta\left(\bar{\rho}_\alpha \bar{U}_\alpha^\beta \bar{U}_\alpha^\nu + \delta^{\beta\nu}\bar{P}_\alpha\right) = L\ \bar{n}_\alpha \bar{q}_\alpha \bar{E}^\nu + L\ \bar{n}_\alpha \bar{q}_\alpha \left(\bar{U}_\alpha \times \bar{B}\right)^\nu\,, \tag{2.13}$$

with

$$L\ = \frac{t_0\, q_0\, B_0}{m_0}\,, \tag{2.14}$$

- **Non-dimensional form of species energy** (2.4)

$$\partial_{\bar{t}}\left(\bar{e}_\alpha\right) + F\ \bar{\nabla}_\beta\left(\bar{U}_\alpha^\beta\left(\bar{e}_\alpha + \bar{P}_\alpha\right)\right) = L\ \bar{n}_\alpha \bar{q}_\alpha \bar{E}_\beta \bar{U}_\alpha^\beta\,, \tag{2.15}$$

- **Non-dimensional form of Ampere's law** (2.9)

$$\partial_t \bar{E}^\nu - A\ \bar{\nabla}_\beta\left(\epsilon^{\nu\,\beta\,\gamma}\bar{B}_\gamma\right) = -C\ \sum_\alpha \bar{n}_\alpha \bar{q}_\alpha \bar{U}_\alpha^\nu\,, \tag{2.16}$$

with

$$A\ = \frac{t_0\, c^2}{U_0\, x_0}\,, \tag{2.17}$$

and

$$C\ = \frac{t_0\, n_0\, q_0}{B_0\, \epsilon_0}\,, \tag{2.18}$$

- **Non-dimensional form of Faraday's Law** (2.6)

$$\partial_t \bar{B}^\nu + F\ \bar{\nabla}_\beta \left(\epsilon^{\nu\,\beta\,\gamma} \bar{E}_\gamma \right) = 0\,, \tag{2.19}$$

- **Non-dimensional form of Poisson's equation** (2.7)

$$\bar{\nabla}_\beta \bar{E}^\beta = C \sum_\alpha \bar{q}_\alpha\, \bar{n}_\alpha\,, \tag{2.20}$$

- **Non-dimensional magnetic flux** (2.8)

$$\bar{\nabla}_\beta \bar{B}^\beta = 0\,. \tag{2.21}$$

In the process of non-dimensionalization, four non-dimensional factors have appeared. These factors will be re-written in terms of the following common plasma physics parameters which are discussed in any book on basic plasma physics [9, 12]. The plasma parameters of interest are described in the following list,

- **Electron thermal speed**

  The electron thermal speed,

$$v_{th\,e} = \left(\frac{2\,P_e}{\rho_e} \right)^{\frac{1}{2}}\,, \tag{2.22}$$

  is the average speed of an electron due to thermal forces. In this case we use the two-dimensional thermal speed which is also the isothermal electron acoustic speed.

- **Ion thermal speed**

  The ion thermal speed,

$$v_{th\,i} = \left(\frac{2\,P_i}{\rho_i} \right)^{\frac{1}{2}}\,, \tag{2.23}$$

  is the average speed of an ion due to thermal forces. The two-dimensional thermal speed is used to eliminate irrational factors in the non-dimensionalization and is the correct speed to use in the calculation of Larmor radius since particles gyrate in a two-dimensional plane.

- **Ion thermal transit time**

  The thermal transit time,

$$\tau_{th\,i} = \frac{x_0}{v_{th\,i}}\,, \tag{2.24}$$

  is the time it takes an thermal ion to travel the distance x_0. The two-dimensional thermal velocity is used for consistency.

- **Light transit time**

  The light transit time,

$$\tau_c = \frac{x_0}{c}\,, \tag{2.25}$$

  is the time it takes electromagnetic waves in free space to propagate the distance x_0

- **Alfven speed**

  The Alfven speed

$$v_{al} = \left(\frac{c^2 \epsilon_0 B_0^2}{n_0 m_i}\right)^{\frac{1}{2}} \tag{2.26}$$

  is the speed of propagation of perturbations in the magnetic field lines of a MHD plasma.

- **Ion plasma frequency**

  The ion plasma frequency,

$$w_{p\,i} = \left(\frac{n_i\, q_i^2}{\epsilon_0\, m_i}\right)^{\frac{1}{2}}\,, \tag{2.27}$$

  is a low frequency oscillation in the ion plasma density.

- **Electron plasma frequency**

  A small perturbation in the electron density of a plasma sets up an oscillation which oscillates at the electron plasma frequency,

$$w_{p\,e} = \left(\frac{n_e\, q_e^2}{\epsilon_0\, m_e}\right)^{\frac{1}{2}}\,. \tag{2.28}$$

  This typically defines smallest important time scale in a plasma except when the speed of light defines a smaller time scale (2.25).

- **Ion cyclotron frequency**

  In the presense of a magnetic field, an ion will gyrate around the magnetic field at the ion cyclotron frequency,

$$w_{c\,i} = \frac{q_i\, B_0}{m_i}\,. \tag{2.29}$$

- **Electron cyclotron frequency**

  In the presence of a magnetic field, an electron will gyrate around the magnetic field at the electron cyclotron frequency,

$$w_{c\,e} = \frac{q_e\, B_0}{m_e}\,. \tag{2.30}$$

- **Ion Larmor radius**

  The ion Larmor radius,

$$r_{g\,i} = \frac{m_i}{q_i}\frac{v_{th\,i}}{B_0}\,, \tag{2.31}$$

  is the radius of gyration of a thermal ion traveling perpendicular to a magnetic field.

- **Electron Larmor radius**

  The electron Larmor radius,

$$r_{g\,e} = \frac{m_e}{q_e}\frac{v_{th\,e}}{B_0}\,, \tag{2.32}$$

  is the radius of gyration of a thermal electron traveling perpendicular to a magnetic field. Recall that in this thesis the two-dimensional thermal speed is used.

- **Debye length**

  The Debye length,

$$\lambda_d = \left(\frac{\epsilon_0\, m_e\, v_{th\,e}^2}{n_0 q_e^2}\right)^{\frac{1}{2}}\,, \tag{2.33}$$

  is the characteristic length at which the potential of a point charge is shield out by the re-arrangement of the plasma around the point charge. This is typically the smallest important length scale in a plasma. Once again, the two-dimensional thermal velocity is used.

In all cases it is assumed that the characteristic velocity of the electron fluid is given by $v_{th\,e} = \left(\frac{m_i}{m_e}\right)^{\frac{1}{2}} v_{th\,i}$. It is possible that $v_{th\,e}$ will be completely independent of the ion characteristic velocity, however, this assumptions simplifies the non-dimensionalization. The non-dimensionalization (2.3.1) given below is used in this thesis when magnetic fields are present. The non-dimensionalization (2.3.2) is used in problems that are essentially electrostatic.

2.3.1 $U_0 = v_{th\,i}$, $t_0 = \frac{x_0}{U_0}$, $E_0 = B_0\,U_0$, $q_0 = q_i$, $m_0 = m_i$

$$L = \tau_{th\,i}\, w_{c\,i} = \frac{x_0}{r_{g\,i}}\,, \tag{2.34}$$

$$C = (\tau_{th\,i}\, w_{p\,i}) \left(\frac{w_{p\,i}}{w_{c\,i}}\right) = \left(\frac{x_0}{\lambda_d}\right) \left(\frac{r_{g\,i}}{\lambda_d}\right)\,, \tag{2.35}$$

$$A = \frac{c^2}{v_{th\,i}^2} = \bar{c}^2\,, \tag{2.36}$$

$$F = 1\,. \tag{2.37}$$

2.3.2 $U_0 = v_{th\,i}$, $t_0 = \frac{x_0}{U_0}$, $B_0 = E_0/U_0$, $E_0 = \frac{m_i\,U_0^2}{q_i\,x_0}$, $q_0 = q_i$, $m_0 = m_i$

$$L = 1\,, \tag{2.38}$$

$$C = \tau_{th\,i}^2\, w_{p\,i}^2 = \left(\frac{x_0}{\lambda_d}\right)^2\,, \tag{2.39}$$

$$A = \frac{c^2}{v_{th\,i}^2} = \bar{c}^2\,, \tag{2.40}$$

$$F = 1\,. \tag{2.41}$$

The non-dimensionalizations (2.3.1) and (2.3.2), suggest that assuming the species charges are equal and opposite, there are four independent parameter which define the type of a problem. They are from (2.3.1), $\frac{\lambda_d}{x_0}$, $\frac{r_{g\,i}}{x_0}$, $\frac{m_i}{m_e}$ and $\frac{v_{th\,i}}{c}$ alternatively $w_{c\,i}$, $w_{p\,i}$, $\tau_{th\,i}$ and $\frac{m_i}{m_e}$. In the remainder of this thesis the bars on the non-dimensional variables will be dropped.

2.4 The MHD Equations

In order to help understand the differences between the two-fluid system of equations and the MHD system of equations, the two-fluid system will be re-written in MHD variables and then the MHD limit will be taken. The various failures of the MHD system can be seen explicitly while helping to explain when the MHD equations do and don't apply. A derivation of ideal MHD can be found in [11], a derivation based on my non-dimensionalization is provided next.

In the following the MHD equations are derived using the non-dimensional variables defined above to show how the MHD limit can be achieved using the two-fluid equations. The following definitions are used

- $n_i = n_e = n$, is the quasi neutrality condition,
- $\rho = \rho_i + \rho_e$,
- $U = U_i + \frac{m_e}{m_i} U_e$,
- $J = n\, q\, (U_i - U_e)$,
- $P = P_i + P_e$, total pressure,
- $e = e_i + e_e$, total energy,
- $\frac{m_e}{m_i} \to 0$, is the massless electron assumption.

The MHD equations are obtained by combining the electron and ion fluid equations and eliminating terms which drop out when $\frac{v_{th\,i}}{c} \to 0$, $\lambda_d \to 0$, and $r_{g\,i} \to 0$.

- **MHD Ampere's Law**

  Letting $\frac{v_{a\,i}}{c} \to 0$ the displacement current disappears, Ampere's Law becomes,

$$\nabla_\beta \left(\epsilon^{\nu\,\beta\,\gamma} B_\gamma \right) = \frac{C}{A}\, J^\nu \,. \tag{2.42}$$

- **MHD Faraday's Law**

  Faraday's Law remains unchanged,

$$\partial_t B^\nu + F\ \nabla_\beta \left(\epsilon^{\nu\,\beta\,\gamma} E_\gamma \right) = 0\,. \tag{2.43}$$

- **MHD Continuity**

  Add the electron and ion continuity equations to get one equation

$$\partial_t \left(\rho \right) + F\ \nabla_\beta \left(\rho U^\beta \right) = 0\,. \tag{2.44}$$

- **MHD Momentum**

  Add the electron and ion momentum equations to get,

$$\rho \frac{d}{dt} U^\nu + F\ \nabla_\beta \left(\delta^{\beta\,\gamma} P \right) = L\, \epsilon^{\nu\,\beta\,\gamma} J_\beta B_\gamma\,, \tag{2.45}$$

  which can be expanded to obtain,

$$\partial_t \left(\rho\, U^\nu \right) + F\ \nabla_\beta \left(\rho\, U^\nu U^\beta + \delta^{\beta\,\gamma} P \right) = L\, \epsilon^{\nu\,\beta\,\gamma} J_\beta B_\gamma\,. \tag{2.46}$$

  Substitute the curl of B for J as in (2.42), to get,

$$\partial_t \left(\rho\, U^\nu \right) + F\ \nabla_\beta \left(\rho\, U^\nu U^\beta + \delta^{\beta\,\gamma} P \right) = \left(\frac{L\ A}{C} \right) \epsilon_{\nu\,\beta\,\gamma} \nabla_\lambda \left(\epsilon^{\beta\,\lambda\,\alpha} B_\alpha \right) B^\gamma\,. \tag{2.47}$$

  Note that,

$$\left(\frac{L\, A}{C} \right) = \left(\frac{v_{al}}{v_{th\,i}} \right)^2\,. \tag{2.48}$$

- **MHD energy**

  Add the electron and ion energy equations to get,

$$\partial_t e + F\ \nabla_\beta \left(U^\beta\, e + U^\beta\, P \right) = L\ E_\beta J^\beta\,. \tag{2.49}$$

Substitute curl B for J as given by (2.42), to get,

$$\partial_t e + F\ \nabla_\beta \left(U^\beta\, e + U^\beta\, P \right) = \left(\frac{L\ A}{C} \right)\ E_\beta \nabla_\nu \left(\epsilon^{\beta\,\nu\,\gamma} B_\gamma \right) . \tag{2.50}$$

- **MHD Ohm's Law**

Multiply the ion momentum equation by $\frac{q}{m_i}$ to get the ion current equation and multiply the electron momentum equation by $-\frac{q}{m_e}$ to get the electron current equation and then add the two equations,

$$\begin{array}{c} \left(\frac{m_e}{q} \right) \left(\frac{1}{L} \right) \frac{d}{dt} J^\nu - \left(\frac{F}{L} \right) \nabla_\beta \left(\delta^{\beta\,\nu} P_e \right) = \\ n\, q \left(E^\nu + \epsilon^{\nu\,\beta\,\gamma} U_\beta B_\gamma \right) - \epsilon^{\nu\,\beta\,\gamma} J_\beta B_\gamma \, . \end{array} \tag{2.51}$$

Substitute curl B for J as given by (2.42), to get,

$$\begin{array}{c} \left(\frac{m_e}{q} \right) \left(\frac{A}{L\ C} \right) \frac{d}{dt} \nabla_\lambda \left(\epsilon^{\beta\,\lambda\,\alpha} B_\alpha \right) - \left(\frac{F}{L} \right) \nabla_\beta \left(\delta^{\beta\,\gamma} P_e \right) = \\ n\, q \left(E^\nu + \epsilon^{\nu\,\beta\,\gamma} U_\beta B_\gamma \right) - \left(\frac{A}{C} \right) \epsilon_{\nu\,\beta\,\gamma} \nabla_\lambda \left(\epsilon^{\beta\,\lambda\,\alpha} B_\alpha \right) B^\gamma \, . \end{array} \tag{2.52}$$

The first term is the rate of change of current,

$$\left(\frac{m_e}{q} \right) \left(\frac{A}{L\ C} \right) \frac{d}{dt} \nabla_\lambda \left(\epsilon^{\beta\,\lambda\,\alpha} B_\alpha \right) , \tag{2.53}$$

with,

$$\frac{A}{L\ C} = \left(\frac{\lambda_d}{x_0} \right)^2 \left(\frac{v_{th\,i}}{c} \right)^2 . \tag{2.54}$$

The second term is the diamagnetic drift,

$$\left(\frac{F}{L} \right) \nabla_\beta \left(\delta^{\beta\,\gamma} P_e \right) , \tag{2.55}$$

with,

$$\left(\frac{F}{L} \right) = \frac{r_{g\,i}}{x_0} , \tag{2.56}$$

and the last term is the Hall current,

$$\left(\frac{A}{C} \right) \epsilon_{\nu\,\beta\,\gamma} \nabla_\lambda \left(\epsilon^{\beta\,\lambda\,\alpha} B_\alpha \right) B^\gamma \tag{2.57}$$

with,

$$\left(\frac{A}{C}\right) = \left(\frac{c}{v_{th\,i}}\right)^2 \left(\frac{\lambda_d^2}{r_{g\,i}\,x_0}\right) . \tag{2.58}$$

2.5 The Ideal MHD Limit

Consider the terms in Ohm's law (2.52) and limits on the parameters λ_d, $r_{g\,i}$. In the case that both $\lambda_d \to 0$ and $r_{g\,i} \to 0$ the rate of change of current (2.53), the diamagnetic drift (2.55) vanish. The Hall current (2.57) vanishes provided $\frac{\lambda_d^2}{r_{g\,i}} \to 0$. This limit is the ideal MHD limit.

The ideal MHD equations are,

- **Ideal MHD Continuity**

$$\partial_t \rho + F\ \nabla_\beta \left(\rho U^\beta\right) = 0\,, \tag{2.59}$$

- **Ideal MHD momentum**

$$\partial_t \left(\rho\, U^\nu\right) + F\ \nabla_\beta \left(\rho\, U^\nu U^\beta + \delta^{\beta\,\gamma} P\right) = \left(\frac{L\ A}{C}\right) \epsilon_{\nu\,\beta\,\gamma} \epsilon^{\beta\,\lambda\,\alpha} B^\gamma\, \nabla_\lambda B_\alpha\,, \tag{2.60}$$

- **Ideal MHD Energy equation**

$$\partial_t e + F\ \nabla_\beta \left(U^\beta\, e + U^\beta\, P\right) = -\left(\frac{L\,A}{C}\right)\ \epsilon^{\beta\,\nu\,\gamma} \epsilon_{\beta\,\lambda\,\kappa}\, U_\nu\, B_\gamma \nabla^\lambda B^\kappa\,, \tag{2.61}$$

- **Ideal MHD Ohm's Law**

$$0 = E^\nu + \epsilon^{\nu\,\beta\,\gamma} U_\beta B_\gamma\,, \tag{2.62}$$

- **Ideal MHD Faraday's Law**

$$\partial_t B^\nu - F\ \nabla_\beta \left(\epsilon^{\nu\,\beta\,\gamma} \epsilon^{\gamma\,\lambda\,\kappa} U_\lambda B_\kappa\right) = 0\,, \tag{2.63}$$

- **Ideal MHD Magnetic Flux**

$$\nabla_\beta B^\beta = 0\,. \tag{2.64}$$

This simple system of equations has been modeled numerically by numerous authors as discussed in the introduction. A homogeneous form of this system exist and it's characteristics are combinations of the fast and slow magnetosonic waves, the Alfven wave and the bulk fluid velocity. The approximation ignores electron plasma waves, cyclotron waves and and electromagnetic waves. Consequently, the system is much less stiff than the two-fluid system and therefore easier to solve numerically. Later on it will be shown that some of the effects that are ignored are significant in certain situations and a two-fluid solution is appropriate in these situations.

2.6 Two-Fluid Dispersion Relations

A number of different waves are described by the two-fluid equations, many of which are not immediately obvious. Although the two-fluid system has only 8 unique characteristics, $\pm c$, U_e, $U_e \pm v_{a\,e}$, U_i, $U_i \pm v_{a\,i}$, a number of dispersive linear waves appear. Any basic plasma text will cover the simple dispersion relations which describe many different waves in a plasma. The derivation of many dispersion relations can be found in [9, 12, 27]. In this section an extensive derivation of plasma waves is developed starting from a linearization of the complete two-fluid system.

The linearized two-fluid equations are obtained by setting

1. $\rho_\alpha = \rho_{\alpha\,0} + \tilde{\rho}_\alpha$,
2. $n_\alpha = n_{\alpha\,0} + \tilde{n}_\alpha$,
3. $U_\alpha^\beta = U_{\alpha\,0}^\beta + \tilde{U}_\alpha^\beta$,
4. $P_\alpha = P_{\alpha\,0} + \tilde{P}_\alpha$,
5. $E^\beta = E_0^\beta + \tilde{E}^\beta$,
6. $B^\beta = B_0^\beta + \tilde{B}^\beta$.

The terms with 0 subscripts are background constants and terms with a tilde are small linear perturbations from the background value. These variables are substituted into the non-linear two-fluid equations and terms that are small, i.e. terms that are a multiple of two or more perturbed quantities, are set to zero. The perturbed variables are assumed to have a linear solution,

1. $\tilde{\rho}_\alpha = \hat{\rho}\, e^{(i\,k(cos(\theta)x+sin(\theta)y+w\,t))}$,
2. $\tilde{n}_\alpha = \hat{n}\, e^{(i\,k(cos(\theta)x+sin(\theta)y+w\,t))}$,
3. $\tilde{U}_\alpha^\beta = \hat{U}_\alpha^\beta\, e^{(i\,k(cos(\theta)x+sin(\theta)y+w\,t))}$,
4. $\tilde{P}_\alpha = \hat{P}_\alpha\, e^{(i\,k(cos(\theta)x+sin(\theta)y+w\,t))}$,
5. $\tilde{E}^\beta = \hat{E}^\beta\, e^{(i\,k(cos(\theta)x+sin(\theta)y+w\,t))}$,
6. $\tilde{B}^\beta = \hat{B}^\beta\, e^{(i\,k(cos(\theta)x+sin(\theta)y+w\,t))}$.

The angle θ is measured between the direction the wave travels and the background magnetic field, $B_0^\beta = (1,0,0)$, which points along the x axis. Without loss of generality the wave vector k^β is assumed to lie in the x, y plane, $k^\beta = k\ (cos\,(\theta)\,, sin\,(\theta)\,, 0)$. The background fluid velocity is assumed to be zero, thus, $U_{\alpha\,0}^\beta = 0$. This assumption is not necessary, but leads to a simpler dispersion relation. Also, $E_0^\beta = 0$ so that no external electric fields are being applied to the fluid. It is assumed that, $P_{e\,0} = P_{i\,0}$, and, $\rho_{e\,0} = \frac{me}{mi}\rho_{i\,0}$, so that the electron fluid and ion fluid have the same background temperature and background number density, $n_{e\,0} = n_{i\,0}$. The electron fluid and ion fluid, however, do have different perturbed number densities and pressures. Using these assumption, the linearized two-fluid equations are as follows,

- **linearized species continuity**

$$w\,\hat{\rho}_\alpha + k_\beta\,\rho_{\alpha\,0}\,\hat{U}_\alpha^\beta = 0\,, \tag{2.65}$$

- **linearized species momentum**

$$i\,w\rho_{\alpha\,0}\hat{U}^{\nu} + i\,k^{\nu}\,P_{\alpha} = n_{\alpha\,0}\,q_{\alpha}\,\left(\hat{E}^{\nu} + \epsilon^{\nu\,\beta\,\gamma}\hat{U}_{\beta}\,B_{\gamma\,0}\right)\,, \tag{2.66}$$

- **linearized species energy**

$$w\,P_{\alpha} + \gamma\,P_0\,k_{\beta}\,\hat{U}^{\beta}_{\alpha} = 0\,, \tag{2.67}$$

- **linearized Ampere's law**

$$i\,w\,\hat{E}^{\nu} - i\,c^2\,k_{\beta}\,\epsilon^{\nu\,\beta\,\gamma}\hat{B}_{\gamma} = -\frac{1}{\epsilon_0}\sum_{\alpha} n_{\alpha\,0}\,q_{\alpha}\,\hat{U}^{\nu}_{\alpha}\,, \tag{2.68}$$

- **linearized Faraday's law**

$$w\,\hat{B}^{\nu} + k_{\beta}\,\epsilon^{\nu\,\beta\,\gamma}\hat{E}_{\gamma} = 0\,. \tag{2.69}$$

The magnetic flux condition and Poisson's equation are not linearized because they contain redundant information. The linear system of equations (2.65)-(2.69), can be written in the matrix form $A\,B = 0$, where,

$$B = \left(\,\hat{n}_e\;\hat{U}_{x\,e}\;\hat{U}_{y\,e}\;\hat{U}_{z\,e}\;\hat{P}_e\;\hat{n}_i\;\hat{U}_{x\,i}\;\hat{U}_{y\,i}\;\hat{U}_{z\,i}\;\hat{P}_i\;\hat{B}_x\;\hat{B}_y\;\hat{B}_z\;\hat{E}_x\;\hat{E}_y\;\hat{E}_z\,\right)^T\,, \tag{2.70}$$

$$A^{1-8} = \begin{pmatrix}
i\,w & i\,n_0\,k\,cos(\theta) & i\,n_0\,k\,sin(\theta) & 0 & 0 & 0 & 0 & 0 \\
0 & i\,n_0\,w & 0 & 0 & \frac{i\,k\,cos(\theta)}{m_e} & 0 & 0 & 0 \\
0 & 0 & i\,n_0\,w & \frac{q}{m_e}\,B_0\,n_0 & \frac{i\,k\,sin(\theta)}{m_e} & 0 & 0 & 0 \\
0 & 0 & -\frac{q}{m_e}\,B_0\,n_0 & i\,n_0\,w & 0 & 0 & 0 & 0 \\
0 & i\,P_0\,\gamma\,k\,cos(\theta) & i\,P_0\,\gamma\,k\,sin(\theta) & 0 & i\,w & 0 & 0 & 0 \\
0 & 0 & 0 & 0 & 0 & i\,w & i\,n_0\,k\,cos(\theta) & i\,n_0\,k\,sin(\theta) \\
0 & 0 & 0 & 0 & 0 & 0 & i\,w & 0 \\
0 & 0 & 0 & 0 & 0 & 0 & 0 & i\,w\,n_0 \\
0 & 0 & 0 & 0 & 0 & 0 & 0 & \frac{q}{m_i}\,B_0\,n_0 \\
0 & 0 & 0 & 0 & 0 & 0 & i\,k\,\gamma\,P_0\,cos(\theta) & i\,k\,\gamma\,P_0\,sin(\theta) \\
0 & 0 & 0 & 0 & 0 & 0 & 0 & 0 \\
0 & 0 & 0 & 0 & 0 & 0 & 0 & 0 \\
0 & 0 & 0 & 0 & 0 & 0 & 0 & 0 \\
0 & -\frac{q\,n_0}{\epsilon_0} & 0 & 0 & 0 & 0 & \frac{q\,n_0}{\epsilon_0} & 0 \\
0 & 0 & -\frac{q\,n_0}{\epsilon_0} & 0 & 0 & 0 & 0 & \frac{q\,n_0}{\epsilon_0} \\
0 & 0 & 0 & -\frac{q\,n_0}{\epsilon_0} & 0 & 0 & 0 & 0
\end{pmatrix}\,, \tag{2.71}$$

and

$$A^{9-16} = \begin{pmatrix} 0 & 0 & 0 & 0 & 0 & 0 & 0 & 0 \\ 0 & 0 & 0 & 0 & 0 & \frac{q}{m_e} n_0 & 0 & 0 \\ 0 & 0 & 0 & 0 & 0 & 0 & \frac{q}{m_e} n_0 & 0 \\ 0 & 0 & 0 & 0 & 0 & 0 & 0 & \frac{q}{m_e} n_0 \\ 0 & 0 & 0 & 0 & 0 & 0 & 0 & 0 \\ 0 & 0 & 0 & 0 & 0 & 0 & 0 & 0 \\ 0 & \frac{i\,k\,cos(\theta)}{m_e} & 0 & 0 & 0 & -\frac{q}{m_i} n_0 & 0 & 0 \\ -\frac{q}{m_i} B_0\, n_0 & \frac{i\,k\,sin(\theta)}{m_i} & 0 & 0 & 0 & 0 & -\frac{q}{m_i} n_0 & 0 \\ i\,w\,n_0 & 0 & 0 & 0 & 0 & 0 & 0 & \frac{q}{m_i} n_0 \\ 0 & i\,w & 0 & 0 & 0 & 0 & 0 & 0 \\ 0 & 0 & i\,w & 0 & 0 & 0 & 0 & i\,k\,sin(\theta) \\ 0 & 0 & 0 & i\,w & 0 & 0 & 0 & i\,k\,cos(\theta) \\ 0 & 0 & 0 & 0 & i\,w & -i\,k\,sin(\theta) & i\,k\,cos(\theta) & 0 \\ 0 & 0 & 0 & 0 & -i\,c^2\,k\,sin(\theta) & i\,w & 0 & 0 \\ 0 & 0 & 0 & 0 & -i\,c^2\,k\,cos(\theta) & 0 & i\,w & 0 \\ \frac{q\,n_0}{\epsilon_0} & 0 & 0 & 0 & i\,c^2\,k\,sin(\theta) & -i\,c^2\,k\,cos(\theta) & 0 & i\,w \end{pmatrix}. \tag{2.72}$$

The solution to this system occurs when $det\,(A) = 0$. The characteristic equation that is obtained gives a dispersion relation which describes the way that linear two-fluid plasma waves propagate. The determinant is written in terms of common two-fluid variables by setting,

1. $P_0 = \frac{v_{a\,e}^2\, n_0\, m_e}{\gamma}$,
2. $n_0 = w_{p\,e}^2 \left(\frac{\epsilon_0\, m_e}{q^2}\right)$,
3. $B_0 = w_{c\,i} \frac{m_i}{q}$,
4. $m_i = \frac{w_{c\,e}}{w_{c\,i}} m_e$.

The dispersion relation written in terms of $w_{c\,i}$, $w_{p\,e}$, $w_{c\,e}$, and $v_{a\,e}$. The result is immediately

divided by the common factor, $\frac{m_e^6\,\epsilon_0^6\,w_{pe}^6}{q^{12}\,w_{ce}^3}$, to obtain[1],

$$\frac{1}{8}\,w^4\,w_{pe}^6\,\Big(-8\,w^4\,\left(w_{ce}+w_{ci}\right)^2\,\left(w^2\,\left(w_{ce}+w_{ci}\right)-2\,v_{ae}^2\,k^2\,w_{ci}\right)\,w_{pe}^6$$
$$+4\,w^2\,\left(w_{ce}+w_{ci}\right)\,\Big(6\,w_{ce}\,\left(w_{ce}+w_{ci}\right)\,w^6+2\,\Big(-v_{ae}^2\,\left(w_{ce}^2+6\,w_{ci}\,w_{ce}+w_{ci}^2\right)\,k^2$$
$$-2\,w_{ce}\,\left(w_{ce}+w_{ci}\right)\,\left(c^2\,k^2+w_{ce}\,w_{ci}\right)\Big)\,w^4+k^2\,w_{ci}\,\Big(2\,k^2\,\left(w_{ce}+w_{ci}\right)\,v_{ae}^4$$
$$+2\,w_{ce}\,\left(4\,c^2\,k^2+3\,w_{ce}\,w_{ci}\right)\,v_{ae}^2+3\,c^2\,w_{ce}^2\,\left(w_{ce}+w_{ci}\right)\Big)\,w^2-4\,v_{ae}^2\,c^2\,k^4\,w_{ce}^2w_{ci}^2\Big)\,w_{pe}^4$$
$$-2\,\left(w-c\,k\right)\,\left(w+c\,k\right)\,w_{ce}\,\Big(12\,w_{ce}\,\left(w_{ce}+w_{ci}\right)\,w^8-4\,\Big(2\,v_{ae}^2\,\left(w_{ce}^2+3\,w_{ci}\,w_{ce}+w_{ci}^2\right)\,k^2$$
$$+w_{ce}\,\left(w_{ce}+w_{ci}\right)\,\Big(c^2\,k^2+\left(w_{ce}+w_{ci}\right)^2\Big)\Big)\,w^6+2\,\Big(c^2\,w_{ce}\,\Big(4\,v_{ae}^2\,w_{ci}\,k^2+\left(w_{ce}+w_{ci}\right)$$
$$\left(w_{ce}^2+w_{ci}\,w_{ce}+w_{ci}^2\right)\Big)\,k^2+w_{ci}\,\Big(4\,v_{ae}^4\,\left(w_{ce}+w_{ci}\right)\,k^4+v_{ae}^2\,w_{ce}$$
$$\left(5\,w_{ce}^2+8\,w_{ci}\,w_{ce}+5\,w_{ci}^2\right)\,k^2+2\,w_{ce}^3\,w_{ci}\,\left(w_{ce}+w_{ci}\right)\Big)\Big)\,w^4+2\,k^2\,w_{ce}\,w_{ci}$$
$$\Big(-2\,k^2\,w_{ci}\,\left(w_{ce}+w_{ci}\right)\,v_{ae}^4-2\,\Big(c^2\,\left(w_{ce}^2+w_{ci}^2\right)\,k^2+w_{ce}^2\,w_{ci}^2\Big)\,v_{ae}^2$$
$$-c^2\,w_{ce}^2\,w_{ci}\,\left(w_{ce}+w_{ci}\right)\Big)\,w^2+3\,v_{ae}^2\,c^2\,k^4\,w_{ce}^3\,w_{ci}^3\Big)\,w_{pe}^2+\left(w-c\,k\right)^2\,\left(w+c\,k\right)^2\,w_{ce}^2$$
$$\Big(8\,w_{ce}\,w^8-8\,\Big(v_{ae}^2\,\left(w_{ce}+w_{ci}\right)\,k^2+w_{ce}\,\left(w_{ce}^2+w_{ci}^2\right)\Big)\,w^6+4\,\Big(2\,v_{ae}^4\,w_{ci}\,k^4$$
$$+v_{ae}^2\,\left(w_{ce}+w_{ci}\right)\,\left(w_{ce}^2+w_{ci}\,w_{ce}+w_{ci}^2\right)\,k^2+2\,w_{ce}^3\,w_{ci}^2\Big)\,w^4-4\,v_{ae}^2\,k^2\,w_{ci}$$
$$\Big(v_{ae}^2\,\left(w_{ce}^2+w_{ci}^2\right)\,k^2+w_{ce}^2\,w_{ci}\,\left(w_{ce}+w_{ci}\right)\Big)\,w^2+3\,v_{ae}^4\,k^4\,w_{ce}^2\,w_{ci}^3\Big)$$
$$-4\,k^2\,w_{ce}^2\,\Big(-w^2\,w_{ci}\,\left(w_{ce}+w_{ci}\right)\,\Big(\left(w^2\,\left(w_{ce}+w_{ci}\right)-4\,v_{ae}^2\,k^2\,w_{ci}\right)\,c^2+2\,v_{ae}^2\,w^2\,w_{ci}\Big)\,w_{pe}^4$$
$$+\left(w-c\,k\right)\,\left(w+c\,k\right)\,\Big(\Big(\left(w_{ce}^3+w_{ci}^3\right)\,w^4-w_{ci}\,\Big(2\,v_{ae}^2\,\left(w_{ce}^2+w_{ci}^2\right)\,k^2$$
$$+w_{ce}^2\,w_{ci}\,\left(w_{ce}+w_{ci}\right)\Big)\,w^2+2\,v_{ae}^2\,k^2\,w_{ce}^2\,w_{ci}^3\Big)\,c^2+v_{ae}^2\,w^2\,w_{ci}$$
$$\left(3\,w^2\,\left(w_{ce}^2+w_{ci}^2\right)-2\,w_{ci}\,\left(v_{ae}^2\,\left(w_{ce}+w_{ci}\right)\,k^2+w_{ce}^2\,w_{ci}\right)\right)\Big)\,w_{pe}^2+$$
$$v_{ae}^2\,\left(w-c\,k\right)^2\,\left(w+c\,k\right)^2\,\Big(-\left(w_{ce}^3+w_{ci}^3\right)\,w^4+w_{ci}\,\Big(v_{ae}^2\,\left(w_{ce}^2+w_{ci}^2\right)\,k^2$$
$$+w_{ce}^2\,w_{ci}\,\left(w_{ce}+w_{ci}\right)\Big)\,w^2-v_{ae}^2\,k^2\,w_{ce}^2\,w_{ci}^3\Big)\Big)\,cos\left(2\,\theta\right)+v_{ae}^2\,k^4\,\left(w-c\,k\right)$$
$$\left(w+c\,k\right)\,w_{ce}^4\,w_{ci}^3\,\Big(v_{ae}^2\,\left(w-c\,k\right)\,\left(w+c\,k\right)-2\,c^2\,w_{pe}^2\Big)\,cos\left(4\,\theta\right)\Big)=0\,. \quad (2.73)$$

(2.73) can be reduced significantly by assuming the waves propagate either parallel or perpendicular to the background magnetic field. Further simplification can be achieved by taking low frequency or high frequency limits. These simplifications follow.

[1]The entire derivation was done using Mathematica and the results copied and pasted into this thesis.

2.6.1 R-mode, L-mode and Alfven waves

The dispersion relation (2.73), can be reduced to a dispersion relation for waves propagating parallel to the background magnetic field by setting $\theta = 0$. The dispersion relation is greatly simplified and the resulting relation for parallel propagating waves is given by

$$\begin{gathered}\left(w_{ce}w^4 - (w_{ce}+w_{ci})\left(v_{ae}^2k^2 + w_{pe}^2\right)w^2 + v_{ae}^2k^2w_{ci}\left(v_{ae}^2k^2 + 2\,w_{pe}^2\right)\right) \\ \left(\left(w^2 - c^2k^2\right)w_{ce}\,(w+w_{ce})\,(w-w_{ci}) - w^2\,(w_{ce}+w_{ci})\,w_{pe}^2\right) \\ \left(\left(w^2 - c^2k^2\right)w_{ce}\,(w-w_{ce})\,(w+w_{ci}) - w^2\,(w_{ce}+w_{ci})\,w_{pe}^2\right) = 0\,.\end{gathered} \tag{2.74}$$

This relation has three different factors, each of which describes a different type of wave. Setting any of these factors to zero is equivalent to solving (2.74). (2.74) can be written as three separate equations which are

$$w_{ce}w^4 - (w_{ce}+w_{ci})\left(v_{ae}^2k^2 + w_{pe}^2\right)w^2 + v_{ae}^2k^2w_{ci}\left(v_{ae}^2k^2 + 2\,w_{pe}^2\right) = 0\,, \tag{2.75}$$

$$\left(w^2 - c^2k^2\right)w_{ce}\,(w+w_{ce})\,(w-w_{ci}) - w^2\,(w_{ce}+w_{ci})\,w_{pe}^2 = 0\,, \tag{2.76}$$

and

$$\left(w^2 - c^2k^2\right)w_{ce}\,(w-w_{ce})\,(w+w_{ci}) - w^2\,(w_{ce}+w_{ci})\,w_{pe}^2 = 0\,. \tag{2.77}$$

In the high frequency limit ion motion is assumed to be negligible and so w_{ci} is set to 0. In this limit, (2.75) reduces to,

$$w^2 = v_{ae}^2k^2 + w_{pe}^2\,, \tag{2.78}$$

which is the electron plasma wave. (2.76) reduces to,

$$w^2 = c^2k^2 + \frac{w\,w_{pe}^2}{w+w_{ce}}\,, \tag{2.79}$$

which is the high frequency L-mode wave. (2.77) reduces to,

$$w^2 = c^2k^2 + \frac{w\,w_{pe}^2}{w-w_{ce}}\,, \tag{2.80}$$

which is the high frequency R-mode wave. These reduced dispersion relations match those described in [9]. In the low frequency limit $w \ll w_{ci} \ll w_{ce}$, (2.75) reduces to,

$$w^2 = v_{ai}^2k^2 + v_{ai}^2k^2\left(\frac{w_{pe}^2}{v_{ae}^2k^2 + w_{pe}^2}\right)\,. \tag{2.81}$$

If $v_{ae}^2 k^2 \ll w_{pe}^2$ this simply becomes,

$$w^2 = 2\, v_{ai}^2 k^2, \tag{2.82}$$

which is the acoustic velocity v_a of the plasma assuming the ion fluid and electron fluid have equal pressures. (2.76) and (2.77), reduce to the equation for the Alfven wave.

$$w^2 = c^2 k^2 \frac{w_{ce} w_{ci}}{w_{pe}^2} = v_{al}^2 k^2 \,. \tag{2.83}$$

with the Alfven speed v_{al} defined as $v_{al}^2 = c^2 \left(\frac{w_{ci}}{w_{pi}}\right)^2$

2.6.2 X-mode, O-mode and Magnetosonic Waves

If θ is set to $\frac{\pi}{2}$ in (2.73) an equation describing wave propagation perpendicular to the background magnetic field is obtained. The dispersion relationship for perpendicular propagating waves is given by,

$$\begin{aligned}
&-(w_{ce}+w_{ci})^2 \left(w^2\,(w_{ce}+w_{ci}) - 2\,v_{ae}^2\,k^2\,w_{ci}\right)\, w_{pe}^6 \\
&+(w_{ce}+w_{ci})\left(3\,w_{ce}\,(w_{ce}+w_{ci})\,w^4 + \left(-v_{ae}^2\,\left(w_{ce}^2+6\,w_{ci}\,w_{ce}+w_{ci}^2\right)\,k^2\right.\right. \\
&\qquad \left.-2\,w_{ce}\,(w_{ce}+w_{ci})\,\left(c^2\,k^2+w_{ce}\,w_{ci}\right)\right)\,w^2 + k^2\,w_{ci} \\
&\qquad \left(k^2\,(w_{ce}+w_{ci})\,v_{ae}^4 + 2\,w_{ce}\,\left(2\,c^2\,k^2+w_{ce}\,w_{ci}\right)\,v_{ae}^2\right. \\
&\qquad \left.\left.+c^2\,w_{ce}^2\,(w_{ce}+w_{ci})\right)\right)\,w_{pe}^4 \\
&-(w-c\,k)\,(w+c\,k)\,w_{ce}\left(3\,w_{ce}\,(w_{ce}+w_{ci})\,w^4\right. \\
&\qquad -\left(2\,v_{ae}^2\,\left(w_{ce}^2+3\,w_{ci}\,w_{ce}+w_{ci}^2\right)\,k^2 + w_{ce}\,(w_{ce}+w_{ci})\right. \\
&\qquad \left.\left(c^2\,k^2+(w_{ce}+w_{ci})^2\right)\right)\,w^2 + w_{ci}\,\left(2\,v_{ae}^2\,k^2 + w_{ce}\,(w_{ce}+w_{ci})\right) \\
&\qquad \left.\left(v_{ae}^2\,(w_{ce}+w_{ci})\,k^2 + w_{ce}\,\left(c^2\,k^2+w_{ce}\,w_{ci}\right)\right)\right)\,w_{pe}^2 \\
&+(w-c\,k)^2\,(w+c\,k)^2\,w_{ce}^2\,\left(w^2 - v_{ae}^2\,k^2 - w_{ce}^2\right) \\
&\qquad \left(w^2\,w_{ce} - w_{ci}\,\left(v_{ae}^2\,k^2 + w_{ce}\,w_{ci}\right)\right) = 0\,.
\end{aligned} \tag{2.84}$$

This relation does not have obvious simple factors so the relation is simplified immediately to obtain high and low frequency limits. In the high frequency limit ion motion is

ignored so $w_{c\,i}$ is set to 0. In this limit the following equation is obtained,

$$\begin{gathered}\left(w^2 - c^2\,k^2 - w_{p\,e}^2\right) \\ \left(w_{p\,e}^4 - \left(2\,w^2 - \left(v_{a\,e}^2 + c^2\right)\,k^2\right)\,w_{p\,e}^2 + (w - c\,k)\,(w + c\,k)\,\left(w^2 - v_{a\,e}^2\,k^2 - w_{c\,e}^2\right)\right) = 0\,.\end{gathered} \tag{2.85}$$

This equation has two factors which when set to zero will satisfy the equation. This leads to two dispersion relations. The first dispersion relation is called the ordinary mode or O-mode dispersion relation,

$$w^2 = c^2k^2 + w_{p\,e}^2\,. \tag{2.86}$$

The second dispersion relation is the extraordinary-mode or X-mode dispersion relation. The X-mode dispersion relation is given by,

$$w^2 = c^2k^2 + w_{p\,e}^2\left(\frac{w^2 - w_{p\,e}^2}{w^2 - w_{c\,e}^2}\right) + w_{p\,e}^2\left(\frac{w^2 - \left(v_{a\,e}^2 + c^2\right)k^2}{w^2 - w_{c\,e}^2}\right)\,. \tag{2.87}$$

If it is assumed that $v_{a\,e} \ll c$ then (2.88) becomes,

$$w^2 = c^2k^2 + w_{p\,e}^2\left(\frac{w^2 - w_{p\,e}^2}{w^2 - w_{c\,e}^2}\right) + w_{p\,e}^2\left(\frac{w^2 - c^2k^2}{w^2 - w_{c\,e}^2}\right)\,. \tag{2.88}$$

which is identical to the X-mode dispersion relation given in [9], although written in a slightly different manner. The Magnetosonic wave can be obtained by letting $r = \frac{m_e}{m_i}$, $w_{p\,e} = w_{c\,i}\,\left(\frac{1}{r}\right)^{\frac{1}{2}}\,\frac{c}{v_a}$, $w_{c\,e} = w_{c\,i}\,\frac{1}{r}$ and $v_{a\,e} = v_{a\,i}\,\left(\frac{1}{r}\right)^{\frac{1}{2}}$ in 2.84. The result is expanded in powers of r and all terms are dropped except those containing the lowest power of r. Eliminating common factors the dispersion relation becomes,

$$\begin{gathered}\left(v_{a\,i}^2\,k^2 - w^2\right)\left(c^2\,k^2\left(v_{a\,i}^2 + v_{al}^2\right) - v_{al}^2\,w^2\right) \\ + \left(c^2 + v_{al}^2\right)\left(c^2\,k^2\left(2\,v_{a\,i}^2 + v_{al}^2\right) - \left(c^2 + v_{al}^2\right)\,w^2\right)\,w_{c\,i}^2 = 0\,.\end{gathered} \tag{2.89}$$

Assuming $w_{c\,i} \to \infty$ the first term can be ignored and the dispersion relation is then,

$$\frac{w^2}{k^2} = c^2\,\frac{2\,v_{a\,i}^2 + v_{al}^2}{c^2 + v_{al}^2}\,, \tag{2.90}$$

which is the same result given in [9].

Chapter 3

NUMERICAL ALGORITHM

3.1 The Two-Fluid System as a Balance Law

A favorite technique of engineers doing research in computational fluid dynamics is the finite volume method based on hyperbolic conservation laws. Starting from this background both Maxwell's equations and the fluid equations have been formulated in the form of conservation laws, or more precisely, balance laws [19] and a finite volume method is used to solve the two-fluid system in one dimension. An outline of the technique for a general conservation laws with source terms follows. The theory of this technique is explained in detail in [19, 18, 28] from which this discussion is derived.

A balance law can be written in the form,

$$\partial_t q^\nu + \nabla_\beta f^{\beta\nu}(q) = \psi^\nu(q) \,, \tag{3.1}$$

with q a vector of conserved variables and f a flux tensor. The script β runs from 1 to 3 while the script ν can be as large as the number of elements in the vector q. (3.1) can be transformed to an integral equation by integrating over an arbitrary volume

$$\int_V \partial_t q^\nu \, dV + \int_V \nabla_\beta f^{\beta\nu}(q) \, dV = \int_V \psi^\nu(q) \, dV \,, \tag{3.2}$$

and using the divergence theorem,

$$\int_V \partial_t q^\nu \, dV + \int_{\partial V} f^{\beta\nu}(q) \, da_\beta = \int_V \psi^\nu(q) \, dV \,. \tag{3.3}$$

This integral form is the basis for the finite volume method. Physically, (3.3), suggests that the rate of change of a quantity inside a volume is equal to the flux of that quantity out of the surface. The two-fluid equations of the previous chapter are written in balance form and can, therefore, be written in this manner. The next step is to discretize the domain of

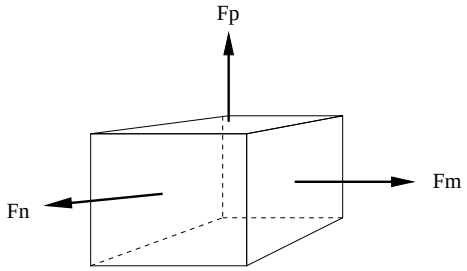

Figure 3.1: Fn, Fm, Fp are fluxes normal to each cell face. In the finite volume method the flux out of each volume is calculated in order to update the solution.

the problem. The simplest discretization is to cut the region of interest into a number of blocks or cells so that the balance law can be updated in each of these cells. See Figure 3.1.

The normal vectors to each cell face are constant everywhere on that face. If the coordinate system is rotated such that the x direction lines up with the cell face normal vector then only the flux in the x direction needs to be calculated because all other fluxes are zero. A one-dimensional Riemann problem is solved across each face to update the solution. With this in mind, the balance law reduces to the following one-dimensional equation

$$\int_V \partial_t q^\nu \, dV + \int_{\partial V} f^{x\,\nu}(q) \, da_x = \int_V \psi^\nu(q) \, dV \, . \tag{3.4}$$

The vector of conserved variables for the electron fluid is,

$$q_e = \begin{pmatrix} \rho_e \\ \rho_e U_{x\,e} \\ \rho_e U_{y\,e} \\ \rho_e U_{z\,e} \\ \frac{1}{2}\rho_e U_{\beta\,e} U_e^\beta + \frac{P_e}{\gamma - 1} \end{pmatrix} = \begin{pmatrix} \rho_e \\ m_{x\,e} \\ m_{y\,e} \\ m_{z\,e} \\ e_e \end{pmatrix} , \tag{3.5}$$

and the corresponding flux in the x direction is given by,

$$f_e = \begin{pmatrix} \rho_e\, U_{x\,e} \\ \rho_e\, U_{x\,e} U_{x\,e} + P_e \\ \rho_e\, U_{y\,e} U_{x\,e} \\ \rho_e\, U_{z\,e} U_{x\,e} \\ U_{x\,e}\,(e_e + P_e) \end{pmatrix} . \tag{3.6}$$

The source vector for the electron fluid equation is given by,

$$\psi_e = \begin{pmatrix} 0 \\ q_e\, n_e\, L\,(E_x + U_{y\,e}\, B_z - U_{z\,e}\, B_y) \\ q_e\, n_e\, L\,(E_y + U_{z\,e}\, B_x - U_{x\,e}\, B_z) \\ q_e\, n_e\, L\,(E_z + U_{x\,e}\, B_y - U_{y\,e}\, B_x) \\ q_e\, n_e\, L\,(E_x\, U_{x\,e} + E_y\, U_{y\,e} + E_z\, U_{z\,e}) \end{pmatrix} . \tag{3.7}$$

The ion conserved variables and flux in the x direction are identical to the electron conserved variables and electron x flux except that the subscript e is replaced with i.

The electromagnetic conserved variable vector is,

$$q_{em} = \begin{pmatrix} B_x \\ B_y \\ B_z \\ E_x \\ E_y \\ E_z \end{pmatrix} , \tag{3.8}$$

with the corresponding flux in the x direction,

$$f_{em} = \begin{pmatrix} 0 \\ -\,E_z \\ E_y \\ 0 \\ -\,c^2\, B_z \\ -\,c^2\, B_y \end{pmatrix} , \tag{3.9}$$

and the source term,

$$\psi_{em} = \begin{pmatrix} 0 \\ 0 \\ 0 \\ C\left(q_e\, n_e\, U_{x\,e} + q_i\, n_i\, U_{x\,i}\right) \\ C\left(q_e\, n_e\, U_{y\,e} + q_i\, n_i\, U_{y\,i}\right) \\ C\left(q_e\, n_e\, U_{z\,e} + q_i\, n_i\, U_{z\,i}\right) \end{pmatrix} . \tag{3.10}$$

Consider only the homogeneous part of each system of equations. The three homogeneous systems are completely decoupled and can be solved independently. It is only through the source terms that the systems interact which provides the option to choose the solver which works best for each of the hyperbolic system. A Roe approximate Riemann Solver is used to solve the homogeneous part of each of the equations.

3.2 Calculating the Homogeneous Flux

The balance law (3.3) is written as the following,

$$\int_V \partial_t q^\nu \, dV + \int_{\partial V} A^\beta_\gamma q^\gamma \, da_\beta = \int_V \psi^\nu \, dV \, . \tag{3.11}$$

The first step is to decompose (3.11) into a system of n linearly independent variables. If f is a nonlinear function of q then the system can only be decomposed locally. For systems that are homogeneous of order one $\left(\frac{\partial f}{\partial q}\right)\left(\frac{\partial q}{\partial x}\right) = \left(\frac{\partial f}{\partial x}\right)$ and A can be chosen to be $\left(\frac{\partial f}{\partial q}\right)$. In cases where f is a linear function of q, as in the case of Maxwell's equations, this choice of A also happens to be a Roe matrix [23]. In general, when f is non-linear a more complicated A matrix must be calculated. The discrete analog of the condition,

$$A\,\frac{\partial\, q}{\partial\, x} = \frac{\partial\, f}{\partial\, x}\,, \tag{3.12}$$

is

$$A\,\Delta_x\, q = \Delta_x\, f\,. \tag{3.13}$$

Roe developed a criteria for constructing such a matrix [23]; the A matrix is called the Roe matrix. The condition on the A matrix is less strict than condition required for true

differentials (3.12). The Roe matrix is important because it reduces the number of calculations necessary to calculate numerical fluxes in the discretized system while satisfying a discrete analog to the continuous condition. The eigenvalues and eigenvectors are calculated from this matrix and a conservative flux function $\tilde{F}$ can be determined. The discretized equation is written,

$$Q^{n+1} = Q^n - \Delta t \frac{A}{V} \left(\tilde{F}^n_{i+1/2} - \tilde{F}^n_{i-1/2} \right) , \tag{3.14}$$

with $\tilde{F}_{i+1/2}$ any chosen explicit numerical flux. The fluxes are defined at the cell centers, but the formulation chosen requires the fluxes at the cell interface. Some approximate flux $\tilde{F}_{i+1/2}$ must be defined at the cell interface. The solution used in this algorithm is the same as that used by Leveque [17]. The numerical flux is a simple first-order upwind flux with a correction flux that adds second order accuracy in smooth regions by the use of flux limiters. The numerical flux given in terms of its Godunov and corrected flux is given by,

$$\tilde{F}_{i+1/2} = F_{i+1/2} + F^c_{i+1/2} , \tag{3.15}$$

with the correction flux F^c defined as,

$$F^c_{i+1/2} = \frac{1}{2} \sum_\nu \left| \lambda^\nu_{j+1/2} \right| \left[1 - \frac{\Delta t}{\Delta x} \left| \lambda^\nu_{j+1/2} \right| \right] \tilde{w}^\nu_{j+1/2} \, r^\nu_{j+1/2} , \tag{3.16}$$

where,

$$F_{i+1/2} = A^+ Q_i + A^- Q_{i+1} , \tag{3.17}$$

and

$$A^+ = \sum_\nu \frac{1}{2} \left(\lambda^\nu_{i+1/2} + \left| \lambda^\nu_{i+1/2} \right| \right) w^\nu_{i+1/2} \, r^\nu_{i+1/2} , \tag{3.18}$$

$$A^- = \sum_\nu \frac{1}{2} \left(\lambda^\nu_{i+1/2} - \left| \lambda^\nu_{i+1/2} \right| \right) w^\nu_{i+1/2} \, r^\nu_{i+1/2} . \tag{3.19}$$

The subscript $i + 1/2$ quantities are interface average quantities. Roe averaging is used for the fluid variables. For the electromagnetic variables arithmetic averaging (taking the average of the quantities at the two adjacent cells) is used which is a Roe average for the electromagnetic system. $\tilde{w}^\nu$ is a flux-limited wave, r^ν is a right eigenvector and λ^ν is the associated eigenvalue.

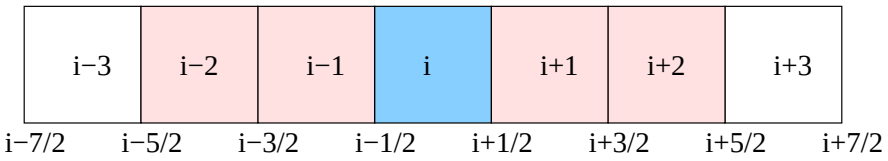

Figure 3.2: Stencil for the calculation of the net flux $\tilde{F}_{i+1/2} - \tilde{F}_{i-1/2}$

The flux-limited right-going wave is defined as,

$$\tilde{w}^{\nu}_{i+1/2} = w^{\nu}_{i+1/2} S(\theta) \ , \tag{3.20}$$

with $w^{\nu}_{i+1/2}$ a wave associated with the eigenvalue $\lambda^{\nu}_{i+1/2}$. The limiter is the minmod limiter defined as,

$$S(\theta) = minmod(1, \theta) \ , \tag{3.21}$$

with θ defined,

$$\theta = \frac{w^{\nu}_{I}}{w^{\nu}_{i}} \, , \tag{3.22}$$

and

$$I = \begin{cases} i + 3/2 & \text{if } \lambda^{\nu} > 0 \\ i - 1/2 & \text{if } \lambda^{\nu} < 0 \end{cases} \ . \tag{3.23}$$

The stencil for a single flux calculation is five wide in one dimension as shown in Figure 3.2. The stencil is passed to a function which calculates both $\tilde{F}_{i-1/2}$ and $\tilde{F}_{i+1/2}$.

For each system a matrix A is calculated as discussed previously. For the fluid systems, A is the Roe matrix [23]. For Maxwell's system, A is simply the Jacobian matrix. The eigenvalues, eigenvectors, and characteristic waves are calculated from the A matrix. Given A, the homogeneous flux can be calculated explicitly as just described.

3.3 Source Treatment

The source terms are calculated in either an explicit or implicit manner. The explicit source is used when the source terms are small compared to the homogeneous fluxes and this algorithm is similar to that described by Schneider and Munz in [25] for their electrostatic

two-fluid code. The implicit source is used when the source terms are of the same magnitude or larger than the homogeneous fluxes. The implicit source helps to ensure numerical stability for stiff problems and can be used any time the explicit source is used. The implicit source is computationally slower than the explicit source. The numerical discretization of the explicit and implicit source is given by,

- explicit source

$$Q^{n+1} = Q^n - \Delta t \frac{A}{V}\left(\tilde{F}^n_{i+1/2} - \tilde{F}^n_{i-1/2}\right) + \Delta t\, \psi^n\,, \tag{3.24}$$

- implicit source

$$Q^{n+1} = Q^n - \Delta t \frac{A}{V}\left(\tilde{F}^n_{i+1/2} - \tilde{F}^n_{i-1/2}\right) + \Delta t\, \psi^{n+1}\,. \tag{3.25}$$

The explicit source is updated simply using the values Q calculated on the previous time step, time step n.

The implicit source is updated using a Newton iteration. The Newton iteration is obtained by expanding ψ^{n+1} in a Taylor series to first order, at which point the discretization can be written,

$$\left(\frac{\partial \psi^k}{\partial Q^k} + \frac{1}{\Delta t}\right)\Delta Q = -\frac{1}{\Delta\, t}\left(Q^k - Q^n\right) - \frac{A}{V}\left(\tilde{F}^n_{i+1/2} - \tilde{F}^n_{i-1/2}\right) + \psi^k\,. \tag{3.26}$$

After the numerical fluxes are calculated explicitly the the source terms are solved implicitly as shown in (3.26). The k index is the kth iteration to convergence. The Jacobian in (3.26) is recalculated and Q is updated after each iteration until the 2-norm of $\Delta\, Q$ has dropped by several orders of magnitude. Inside each iteration the linear system, (3.26), is solved using about three symmetric Gauss-Seidel steps. It is important to note that $\frac{\partial \psi^k}{\partial Q^k}$ is local; ψ does not depend on the value of Q in neighboring cells. This means that the computational work required to solve (3.26) increases linearly with the number of cells in the domain, even if the scheme is extended to three dimensions.

Because ψ is a simple algebraic function of Q, the Jacobian is calculated analytically. Eleven of the sixteen equations have non-zero source terms and these equations must be

updated implicitly. The full Jacobian is a 11×11 matrix. In many cases of interest the electron source terms are much stiffer than the ion source terms and a second Jacobian matrix is used consisting of only the electromagnetic and electron equations. This system requires a 7×7 Jacobian matrix. The electromagnetic and electron equations are solved implicitly at every step while the full system (electromagnetic, electron, ion) is updated implicitly periodically. The bottleneck in the algorithm becomes the implicit solution of the electromagnetic and electron equations. Speed up can be obtained by updating the electromagnetic terms explicitly for several steps and then updating the electron equation with the electromagnetic equation implicitly every few steps. The stability of this last technique is unpredictable and even when the solution remains stable, unphysical oscillations can appear. In general, it is better to solve for the electrons and electromagnetic field implicitly at every step.

The full implicit conserved variable vector is,

$$Q = \begin{pmatrix} m_{x\,e} & m_{y\,e} & m_{z\,e} & e_e & m_{x\,i} & m_{y\,i} & m_{z\,i} & e_i & E_x & E_y & E_z \end{pmatrix}^T . \tag{3.27}$$

Letting $r_e = q_e/m_e$ and $r_i = q_i/m_i$ the source terms associated with these 11 variables are,

$$\psi = \begin{pmatrix} L\, r_e\, (\rho_e\, E_x + m_{y\,e}\, B_z - m_{z\,e}\, B_y) \\ L\, r_e\, (\rho_e\, E_y - m_{x\,e}\, B_z + m_{z\,e}\, B_x) \\ L\, r_e\, (\rho_e\, E_z + m_{x\,e}\, B_y - m_{y\,e}\, B_x) \\ L\, r_e\, (m_{x\,e}\, E_x + m_{y\,e}\, E_y + m_{z\,e}\, E_z) \\ L\, r_i\, (\rho_i\, E_x + m_{y\,i}\, B_z - m_{z\,i}\, B_y) \\ L\, r_i\, (\rho_i\, E_y - m_{x\,i}\, B_z + m_{z\,i}\, B_x) \\ L\, r_i\, (\rho_i\, E_z + m_{x\,i}\, B_y - m_{y\,i}\, B_x) \\ L\, r_i\, (m_{x\,i}\, E_x + m_{y\,i}\, E_y + m_{z\,i}\, E_z) \\ C\, (r_i\, m_{x\,i} + r_e\, m_{x\,e}) \\ C\, (r_i\, m_{y\,i} + r_e\, m_{y\,e}) \\ C\, (r_i\, m_{z\,i} + r_e\, m_{z\,e}) \end{pmatrix} . \tag{3.28}$$

The source Jacobian matrix $\frac{\partial \psi}{\partial Q}$ is,

$$\begin{pmatrix}
0 & L\,r_e\,B_z & -L\,r_e\,B_y & 0 & 0 & 0 & 0 & 0 & L\,r_e\,\rho_e & 0 & 0 \\
-L\,r_e\,B_z & 0 & L\,r_e\,B_x & 0 & 0 & 0 & 0 & 0 & 0 & L\,r_e\,\rho_e & 0 \\
L\,r_e\,B_y & -L\,r_e\,B_x & 0 & 0 & 0 & 0 & 0 & 0 & 0 & 0 & L\,r_e\,\rho_e \\
L\,r_e\,E_x & L\,r_e\,E_y & L\,r_e\,E_z & 0 & 0 & 0 & 0 & 0 & L\,r_e\,m_{x\,e} & L\,r_e\,m_{y\,e} & L\,r_e\,m_{z\,e} \\
0 & 0 & 0 & 0 & 0 & L\,r_i\,B_z & -L\,r_i\,B_y & 0 & L\,r_i\,\rho_i & 0 & 0 \\
0 & 0 & 0 & 0 & -L\,r_i\,B_z & 0 & L\,r_i\,B_x & 0 & 0 & L\,r_i\,\rho_i & 0 \\
0 & 0 & 0 & 0 & L\,r_i\,B_y & -L\,r_i\,B_x & 0 & 0 & 0 & 0 & L\,r_i\,\rho_i \\
0 & 0 & 0 & 0 & -L\,r_i\,E_x & -L\,r_i\,E_z & 0 & L\,r_i\,m_{x\,i} & L\,r_i\,m_{y\,i} & L\,r_i\,m_{z\,i} & \\
-C\,r_e & 0 & 0 & 0 & -C\,r_i & 0 & 0 & 0 & 0 & 0 & 0 \\
0 & -C\,r_e & 0 & 0 & 0 & -C\,r_i & 0 & 0 & 0 & 0 & 0 \\
0 & 0 & -C\,r_e & 0 & 0 & 0 & -C\,r_i & 0 & 0 & 0 & 0
\end{pmatrix}. \tag{3.29}$$

The electromagnetic and electron source Jacobian $\frac{\partial \psi}{\partial Q}$ is,

$$Q = \begin{pmatrix} m_{x\,e} & m_{y\,e} & m_{z\,e} & e_e & E_x & E_y & E_z \end{pmatrix}^T, \tag{3.30}$$

and the related source terms are,

$$\psi = \begin{pmatrix}
L\,r_e\,(\rho_e\,E_x + m_{y\,e}\,B_z - m_{z\,e}\,B_y) \\
L\,r_e\,(\rho_e\,E_y - m_{x\,e}\,B_z + m_{z\,e}\,B_x) \\
L\,r_e\,(\rho_e\,E_z + m_{x\,e}\,B_y - m_{y\,e}\,B_x) \\
L\,r_e\,(m_{x\,e}\,E_x + m_{y\,e}\,E_y + m_{z\,e}\,E_z) \\
C\,(r_i\,m_{x\,i} + r_e\,m_{x\,e}) \\
C\,(r_i\,m_{y\,i} + r_e\,m_{y\,e}) \\
C\,(r_i\,m_{z\,i} + r_e\,m_{z\,e})
\end{pmatrix}, \tag{3.31}$$

with their associated Jacobian matrix defined as,

$$\left(\frac{\partial \psi}{\partial Q}\right) = \begin{pmatrix}
0 & L\,r_e\,B_z & -L\,r_e\,B_y & 0 & L\,r_e\,\rho_e & 0 & 0 \\
-L\,r_e\,B_z & 0 & L\,r_e\,B_x & 0 & 0 & L\,r_e\,\rho_e & 0 \\
L\,r_e\,B_y & -L\,r_e\,B_x & 0 & 0 & 0 & 0 & L\,r_e\,\rho_e \\
L\,r_e\,E_x & L\,r_e\,E_y & L\,r_e\,E_z & 0 & L\,r_e\,m_{x\,e} & L\,r_e\,m_{y\,e} & L\,r_e\,m_{z\,e} \\
-C\,r_e & 0 & 0 & 0 & 0 & 0 & 0 \\
0 & -C\,r_e & 0 & 0 & 0 & 0 & 0 \\
0 & 0 & -C\,r_e & 0 & 0 & 0 & 0
\end{pmatrix}. \tag{3.32}$$

3.4 Stability

The scalar equation,

$$\partial_t\,u + a\,\partial_x u = i\,\lambda\,u \tag{3.33}$$

may be a good model for the two-fluid system in terms of numerical stability. The above describes a wave equation with an oscillating source term provide λ is real. A Von-Neumann stability analysis of this equation using the explicit scheme shows that the explicit scheme

is amplifying, this is in agreement with the observed behavior of the explicit scheme applied to the non-linear system. However, for problems which aren't too stiff, solutions can be obtained faster with the explicit scheme than with the implicit scheme. Step for step the explicit scheme is about 30% faster than the implicit scheme. The problem is that given enough time, the explicit scheme will always go unstable because it is amplifying.

The implicit scheme has a definite stability region which corresponds to significant two-fluid plasma parameters. The fluid equations produce the characteristics

$$U, \quad U + \left(\frac{\gamma P}{\rho}\right)^{\frac{1}{2}}, \quad U - \left(\frac{\gamma P}{\rho}\right)^{\frac{1}{2}} \quad , \tag{3.34}$$

while Maxwell's equations produce the characteristics $\pm c$. If it weren't for the source terms the time step for a simulation could be based on the Courant number $\Delta t \frac{A}{V} |\nu| < 1$ where ν is the fastest characteristic. However, as has already been stated, the two-fluid system admits many additional linear waves. Two waves in particular, the electron cyclotron wave (2.30), and the electron plasma wave (2.28) must be resolved in order for the system to be stable. For stability the smaller time scale calculated from the Courant condition, the electron plasma frequency (2.28), and the electron cyclotron frequency (2.30), must be chosen. When the electron cyclotron frequency and the electron plasma frequency are of the same magnitude, the necessary time scale is defined by the upper hybrid frequency $w_{UH}^2 = w_{ce}^2 + w_{pe}^2$. The necessary spatial scale depends on the existence of shocks. In the presence of shocks, spatial scales on the order of a Debye length (2.33), appear to be necessary for accurate solutions although they are not required for stability. This is an issue which will require more research.

3.5 Boundary Conditions

All the simulations used in this thesis use the most simple boundary conditions, either copy or periodic. The copy boundary condition simply copies the data at the very edge of the computational domain onto the boundary. Periodic boundary conditions copy the edge data from the left half of the domain to the right half of the domain and visa versa.

Chapter 4

SIMULATIONS

4.1 Debye Shielding

If a point charge is introduced into a plasma, the plasma will quickly surround the charge in a manner that shields out the charge in approximately one Debye length. This simulation uses the correction potential (2.20), (2.9), to maintain a potential in the middle of the domain. The fluids move around and eventually shield out the electric field as predicted by theory. The problem was run until numerical dissipation brought the simulation to steady state. Figures 4.1, 4.2 and 4.3 show the charge distribution, the electric field, and the correction potential at steady state, respectively.

The correction potential has been tried on a number of other problems without much success. As a result, the correction potential is not used in the remainder of the simulations. For fixed background charges a much simpler method can be used to ensure that the background electric field does not decay away. Specifically a permanent background electric field can be defined and the correction potential can be removed.

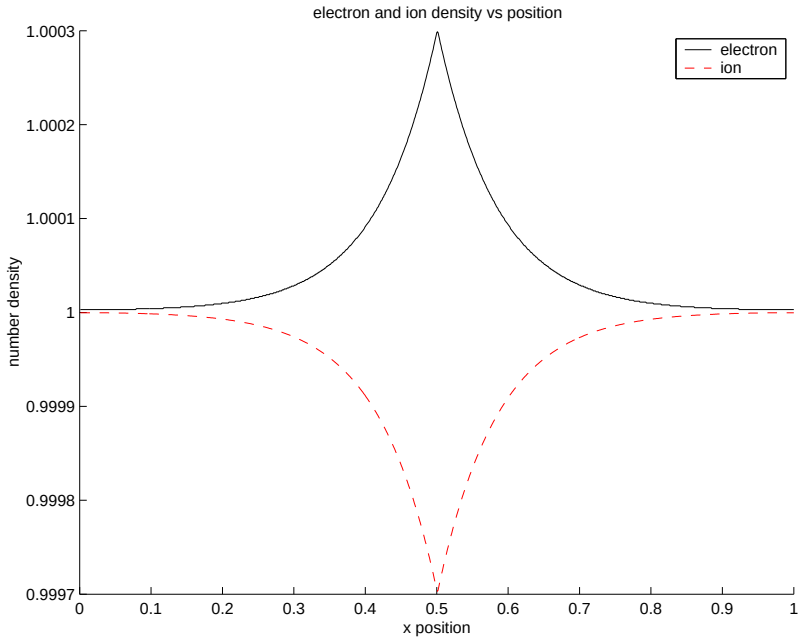

Figure 4.1: Steady state charge distribution for the Debye shielding problem. This diagram shows the fluids in steady state after they have moved from and initially uniform distribution. The electron fluid is attracted to the charge while the ion fluid is repelled.

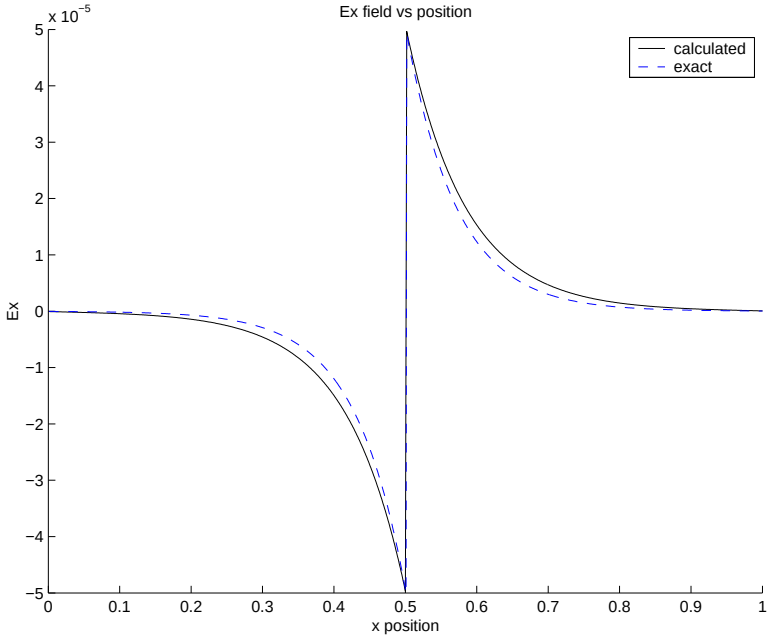

Figure 4.2: Steady state E_x distribution for the Debye shielding problem. This plot shows the steady state electric field decaying away from the shielded point charge. The analytic results assumes heat conduction, our plasma model does not include heat conduction and so the steady state solution is slightly different from the analytic solution.

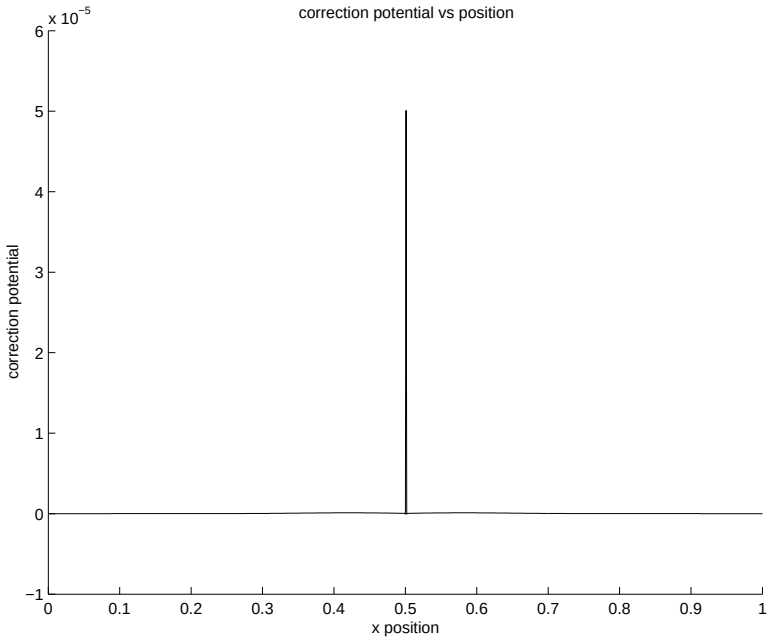

Figure 4.3: Steady state correction potential for the Debye shielding problem. The correction potential propagates out of the domain so at steady state there is only a potential spike at the point where the point charge exists.

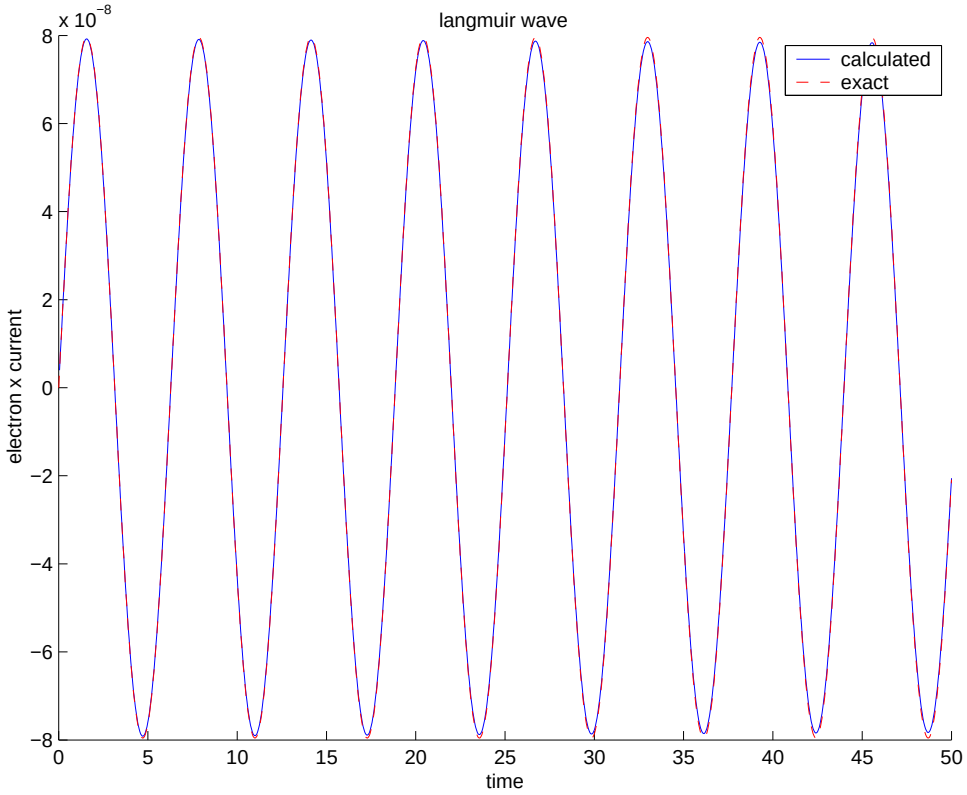

Figure 4.4: Electron current verses time for an electron plasma wave. A small sinusoidal electron density perturbation was set up in the domain. The time evolution of velocity at a point in the middle of the domain is measured and plotted in this figure. The analytic and calculated solutions agree.

4.2 Electron Plasma Waves

Electron plasma waves or Langmuir waves are electrostatic stationary electron waves that are not seen in the MHD equations. The electron plasma frequency is a function of plasma density (2.28) and is used to determine the density of plasma in the upper atmosphere. Electromagnetic waves with frequency less than the Langmuir frequency cannot propagate in a plasma because the electrons adjust quickly enough to cancel out the electric fields in the waves. The Langmuir frequency can be obtained from the dispersion relation derived from the linearized two fluid equations.

The electron plasma wave simulation was performed with negligible temperature using the implicit and explicit schemes. The implicit scheme gives rise to a slowly decaying solution while the explicit scheme gives rise to a slowly amplifying solution. A calculated verses exact solution for a Langmuir wave is plotted in Figure 4.4.

4.3 Electromagnetic Shock

As has already been discussed, the MHD equations are a limiting case of the two-fluid equations. A number of plasmas of interest including fusion plasmas fall into a regime where Debye length and Larmor radius are small. This makes the MHD model a reasonably accurate approximation to the plasma physics involved, however, as will be shown, the MHD model still misses potentially important phenomena even when the Debye length and Larmor radius are small. In addition it will be shown how the two-fluid solution varies as the Debye length and Larmor radius are changed. Here the well known Brio and Wu shock [7] is solved with finite Debye length and Larmor radius. The solutions are compared to the limiting cases of MHD and gas dynamic shocks.

The non-dimensionalization given in section 2.3.1 is used. In the following $v_{th\,i} = 1$ and $c = 100$. In these simulations $\frac{m_i}{m_e} = 1836$ and $q_i = -q_e = 1$ and $\lambda_d = \frac{1}{100} r_{g\,i}$.

The ideal MHD system uses the following variable definitions with respect to the two-fluid system,

$$\begin{pmatrix} \rho \\ v_x \\ v_y \\ v_z \\ P \\ B_x \\ B_y \\ B_z \end{pmatrix} = \lim_{\frac{m_e}{m_i} \to 0} \begin{pmatrix} \rho_i + \rho_e \\ \frac{\rho_i\, v_{x\,i} + \rho_e\, v_{x\,e}}{\rho_i + \rho_e} \\ \frac{\rho_i\, v_{y\,i} + \rho_e\, v_{y\,e}}{\rho_i + \rho_e} \\ \frac{\rho_i\, v_{z\,i} + \rho_e\, v_{z\,e}}{\rho_i + \rho_e} \\ P_i + P_e \\ B_x \\ B_y \\ B_z \end{pmatrix} = \begin{pmatrix} \rho_i \\ v_{x\,i} \\ v_{y\,i} \\ v_{z\,i} \\ P_i + P_e \\ B_x \\ B_y \\ B_z \end{pmatrix}. \tag{4.1}$$

The shock used here is identical to the Brio and Wu shock except that the ratio of the ion acoustic velocity to the speed of light must be specified.

Initial conditions on the left half of the MHD shock are,

$$L_{MHD} = \begin{pmatrix} \rho \\ v_x \\ v_y \\ v_z \\ P \\ B_x \\ B_y \\ B_z \end{pmatrix} = \begin{pmatrix} 1.0 \\ 0 \\ 0 \\ 0 \\ 1.0 \\ 0.75 \\ 1.0 \\ 0 \end{pmatrix}, \tag{4.2}$$

and on the right

$$R_{MHD} = \begin{pmatrix} \rho \\ v_x \\ v_y \\ v_z \\ P \\ B_x \\ B_y \\ B_z \end{pmatrix} = \begin{pmatrix} 0.125 \\ 0 \\ 0 \\ 0 \\ 0.1 \\ 0.75 \\ -1.0 \\ 0 \end{pmatrix}. \tag{4.3}$$

The equivalent initial conditions for the two-fluid shock follow. L are the initial conditions on the left half of the shock and R are the initial conditions on the right half of the

shock. L and R are given by,

$$L = \begin{pmatrix} \rho_e \\ v_{x\,e} \\ v_{y\,e} \\ v_{z\,e} \\ p_e \\ \rho_i \\ v_{x\,i} \\ v_{y\,i} \\ v_{z\,i} \\ p_i \\ B_x \\ B_y \\ B_z \\ E_x \\ E_y \\ E_z \end{pmatrix} = \begin{pmatrix} 1.0\,\frac{m_e}{m_i} \\ 0 \\ 0 \\ 0 \\ 0.5 \\ 1.0 \\ 0 \\ 0 \\ 0 \\ 0.5 \\ 0.75 \\ 1.0 \\ 0 \\ 0 \\ 0 \\ 0 \end{pmatrix}, \quad R = \begin{pmatrix} \rho_e \\ v_{x\,e} \\ v_{y\,e} \\ v_{z\,e} \\ p_e \\ \rho_i \\ v_{x\,i} \\ v_{y\,i} \\ v_{z\,i} \\ p_i \\ B_x \\ B_y \\ B_z \\ E_x \\ E_y \\ E_z \end{pmatrix} = \begin{pmatrix} 0.125\,\frac{m_e}{m_i} \\ 0 \\ 0 \\ 0 \\ 0.05 \\ 0.125 \\ 0 \\ 0 \\ 0 \\ 0.05 \\ 0.75 \\ -1.0 \\ 0 \\ 0 \\ 0 \\ 0 \end{pmatrix}. \tag{4.4}$$

The initial conditions for the total fluid number density will differ slightly from the MHD density because the electrons have finite mass.

4.3.1 MHD limit: $r_{g\,i} \to 0,\ \lambda_d \to 0$

With the two-fluid system the true MHD limit cannot be achieved because the stiffness of the problem increases with decreasing Larmor radius. This is apparent because $w_{p\,e}$ increases and thus the time step that needs to be resolved becomes smaller. In the true MHD limit the time step would drop to zero and no solution could be obtained. In addition the spatial scale that needs to be resolved decreases as some multiple of the Debye length, and so the grid resolution would become infinitely large. Running simulations on a single machine over the course of about five days, the following two-fluid results to the shock problem were obtained with $r_{g\,i} = \frac{1}{300}$ and $\lambda_d = \frac{1}{30000}$ while the number of grid cells is 4000.

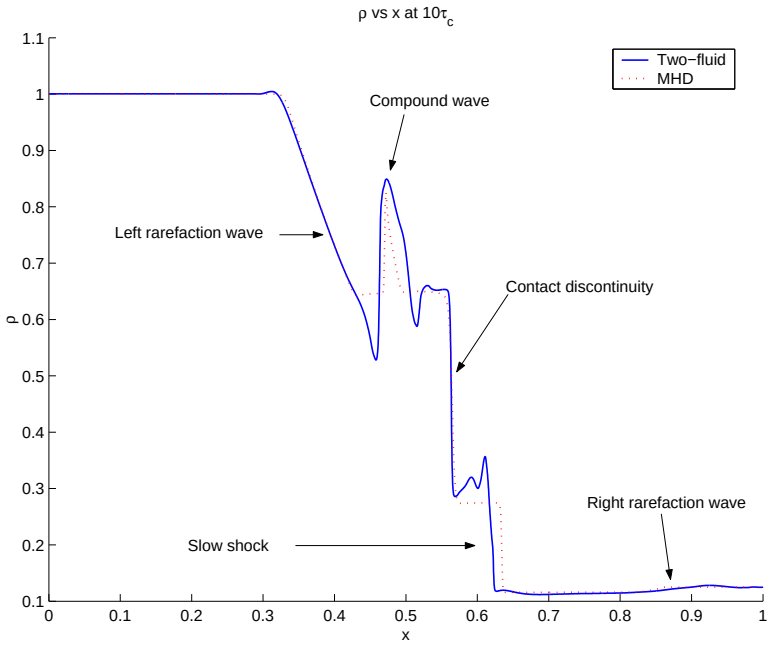

Figure 4.5: Two-fluid density profile for $r_{g\,i} = \frac{1}{300}$ verses the MHD solution. The contact discontinuity, right rarefaction wave, left rarefaction wave and compound wave are well resolved in the two-fluid solution, but the slow shock is traveling slightly slower in the two-fluid solution than it is in the MHD solution. It is not clear whether or not this problem will be resolved with smaller $r_{g\,i}$ and higher grid resolution.

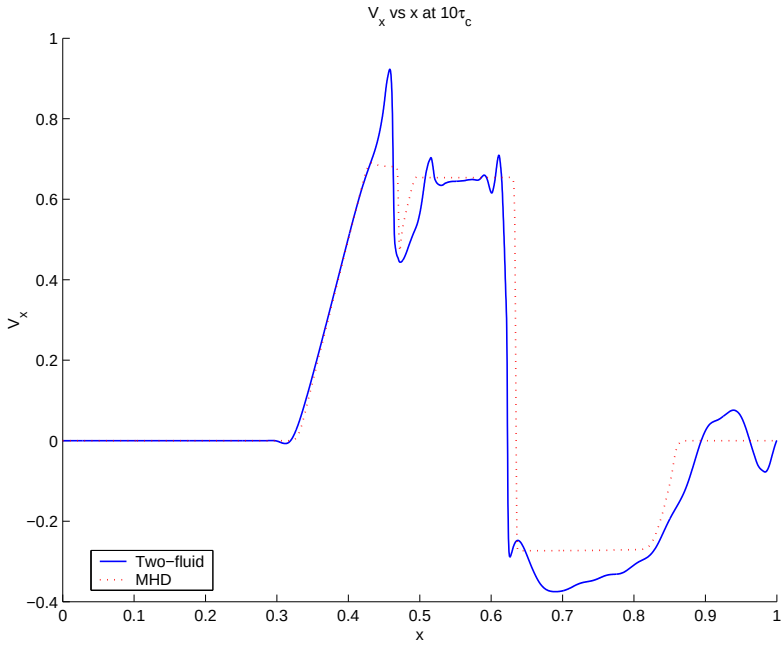

Figure 4.6: Two-fluid V_x profile for $r_{g\,i} = \frac{1}{300}$ verses the MHD solution. V_x originates at the shock front in both the MHD and two-fluid shock solutions. The Larmor radius is slightly larger on the right hand side of the shock, therefore, the right hand side of the two-fluid solution will differ from the Ideal MHD solution. Low frequency waves are seen on the right hand side.

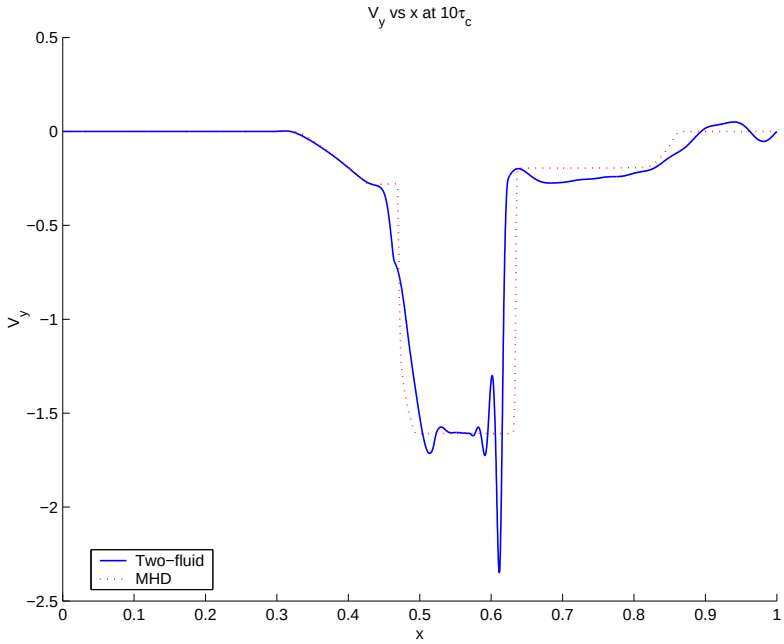

Figure 4.7: Two-fluid V_y profile for $r_{g\,i} = \frac{1}{300}$ verses the MHD solution. This figure shows that a shock induces a V_y in both the MHD and two-fluid solution. The sharp spikes in the two-fluid solution support the B_z magnetic field induced by the Hall term.

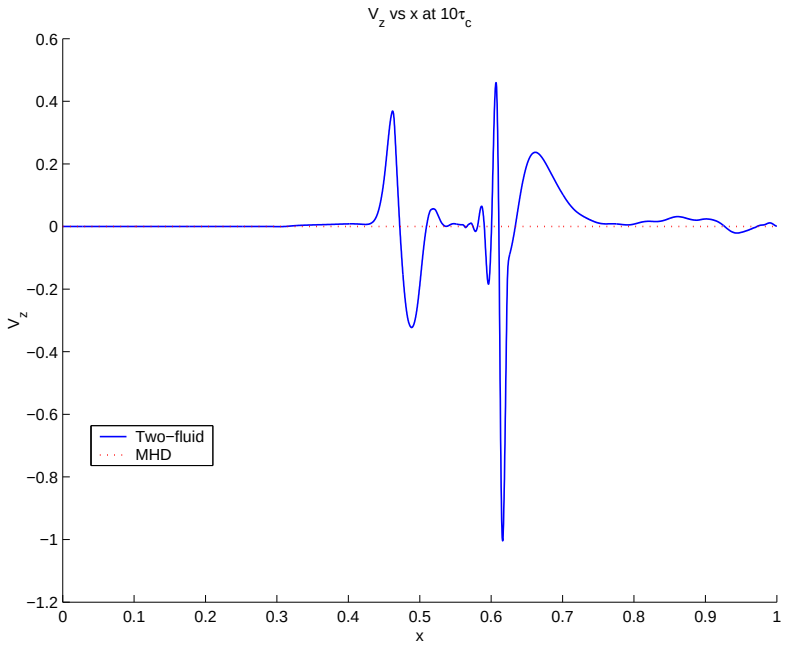

Figure 4.8: Two-fluid V_z profile for $r_{gi} = \frac{1}{300}$ verses the MHD solution. This figure of V_z gives the first indication that the two-fluid solution differs substantially from the MHD solution. In the two-fluid system the magnetic field is different from the fluid current because displacement current is not ignored. As a result a fluid current is necessary to support the shock in B_y. The two-fluid equations show net velocity in the y direction when the ideal MHD equations suggest there should be no such velocity. This points to one additional problem with numerically modeling the two-fluid system. In the limit of small Larmor radii, a true magnetic shock must be supported by a delta function in J. Not only is it necessary to resolve shocks, it is also necessary to resolve current spikes which become delta functions in the MHD limit.

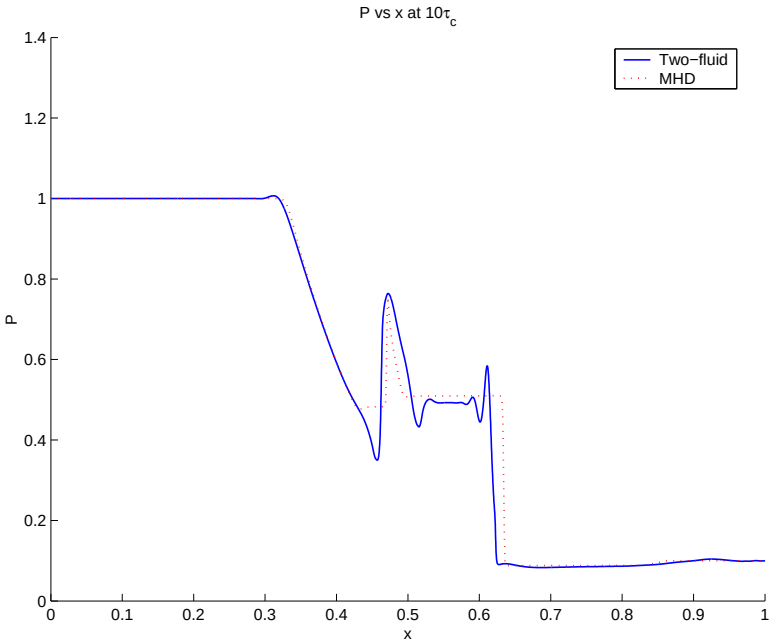

Figure 4.9: Two-fluid P profile for $r_{g\,i} = \frac{1}{300}$ verses the MHD solution. The pressure profile is comparable for the two-fluid solution and the MHD solution. Features similar to those in Figure 4.5 appear.

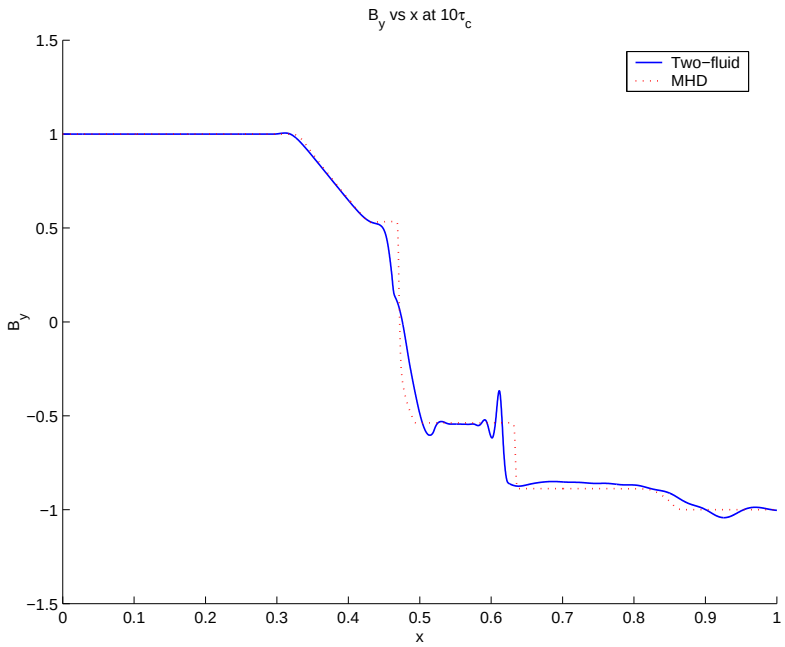

Figure 4.10: Two-fluid B_y profile for $r_{g\,i} = \frac{1}{300}$ verses the MHD solution. An additional structure in B_y appears to be forming in the two-fluid solution near the center of the domain.

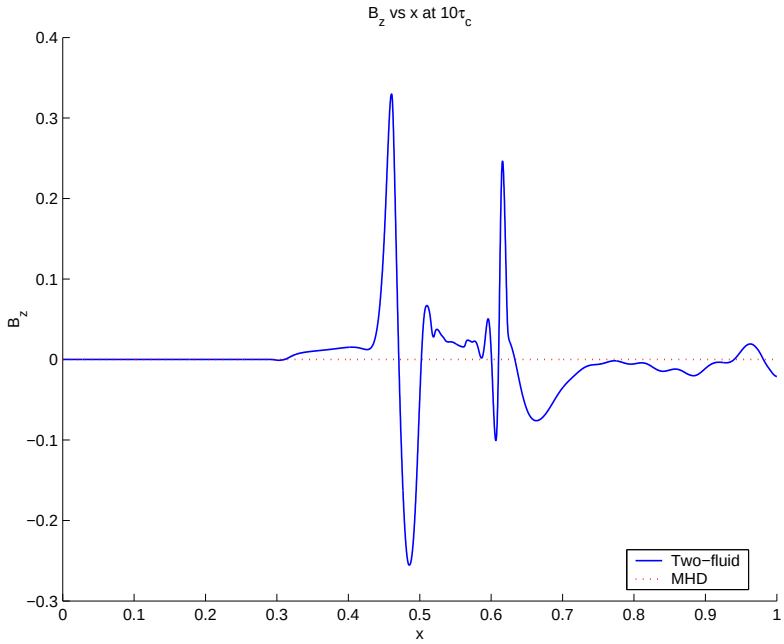

Figure 4.11: Two-fluid B_z profile for $r_{g\,i} = \frac{1}{300}$ verses the MHD solution. The Hall term has created a B_z in the two-fluid solution. The sharp spikes are necessary to support the current in the y direction

4.3.2 Non-neutral gas dynamic limit: $r_{g\,i} \to \infty$, $r_{g\,e} \to \infty$, $\lambda_d \to \infty$

In this case by setting $q = 0$ the non-neutral gas dynamic limit can be achieved. This limit is called non-neutral because the electrons are not bound to the ions, large charge separation occurs and the simulation is sub-Debye length. In this sense, this simulation is non-physical because in most cases it is likely that the fluid equations do not apply in this regime, i.e. a particle approach would be required. However, in this regime, the two-fluid equations predict a shock structure that is identical to that of gas dynamics and it is the purpose of this section to show that this is in fact the solution that is obtained. In Figures 4.12-4.14, notice that the electron fluid is plotted at a different time than the ion fluid. Figure 4.12 shows the number density profile of ions verses electrons. Figure 4.13 shows the electron and ion V_x distribution. Figure 4.14 shows the electron and ion pressure distribution. All three figures show exactly gas dynamic structure. In Figure 4.15 the simulation produces and electromagnetic shock which is identical to the solution predicted by the sourceless Maxwell's equations. Figures 4.12-4.15 illustrate that in the limit of large $r_{g\,i}$ and large λ_d the two-fluid equations reduce to a pair of sourceless fluid equations and sourceless Maxwell's equations. Additional simulations will show more physically realistic solutions which lie between the MHD and non-neutral gas dynamic limits.

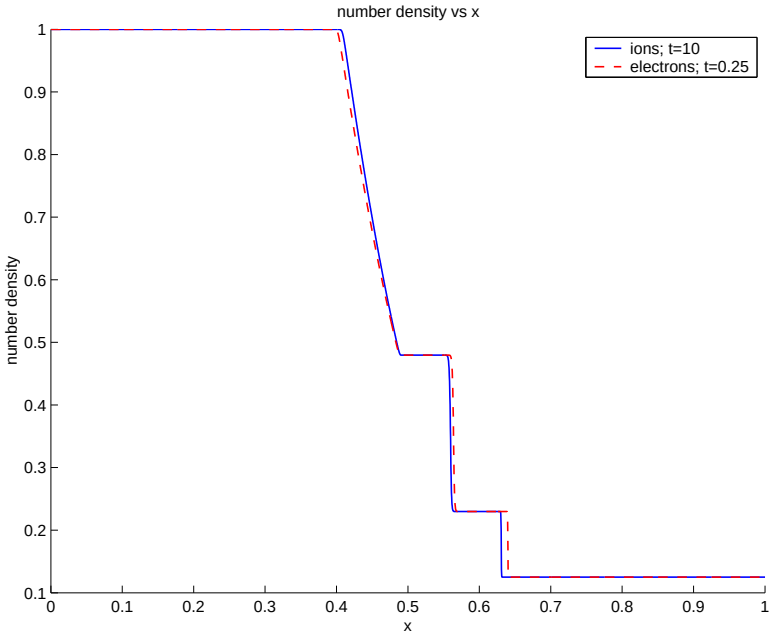

Figure 4.12: Number density in the non-neutral gas dynamic limit. This figure is deceiving because the electron number density is plotted at a different time than the ion number density (notice the legend). The electrons travel much faster than the ions because of their reduced mass. The electron shock quickly leaves the domain and the electrons reach an equilibrium before the ions reach the end of the domain. In this case large charge separation occurs because the fields that develop are negligible.

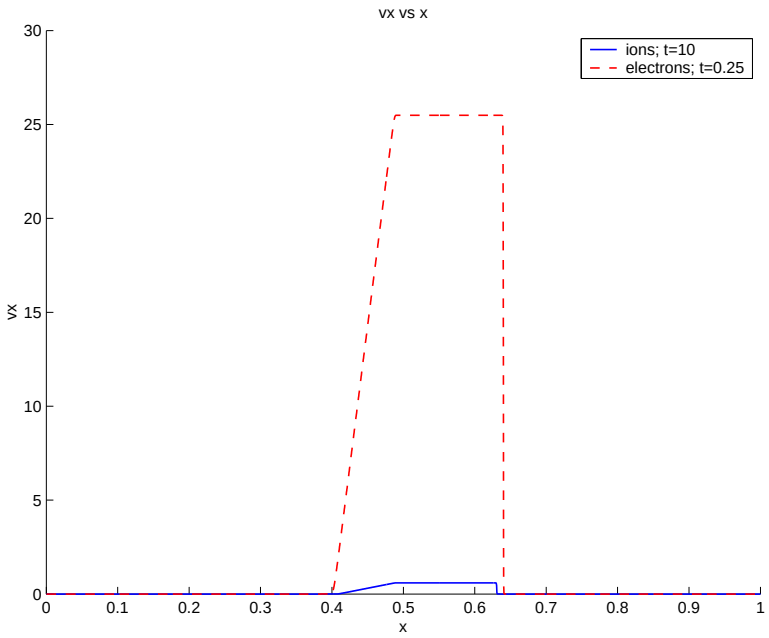

Figure 4.13: V_x in the non-neutral gas dynamic limit. This figure shows the electron and ion fluid V_x. When the electrons are not bound to the ions they move at the electron acoustic speed which approaches the speed of light. Recall that the speed of light for these simulations is 100. In future algorithms it may be appropriate to formulate the electrons relativistically because they can reach such high speeds.

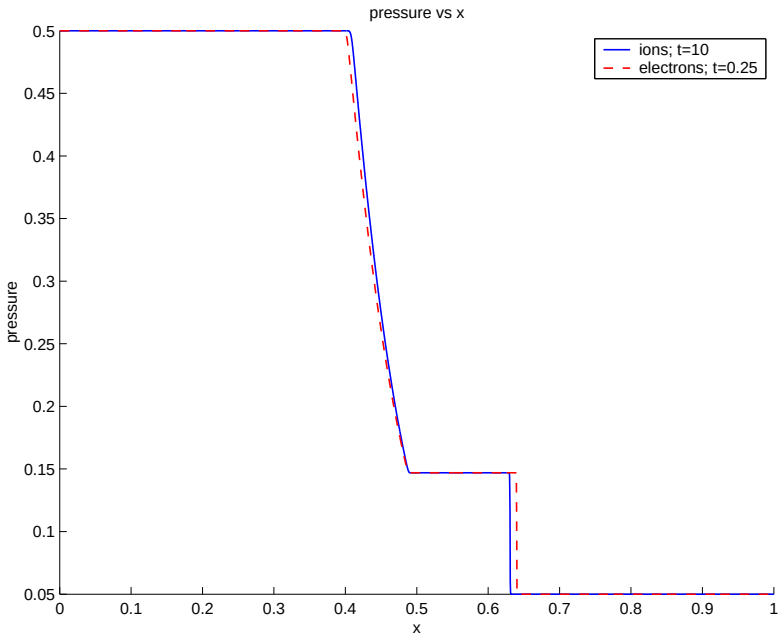

Figure 4.14: Pressure in the non-neutral gas dynamic limit. Initially the pressure distribution is set evenly between the electrons and ions. Because the two fluids are identical except for particle mass, the pressure profiles have identical structure, but evolve at different rates.

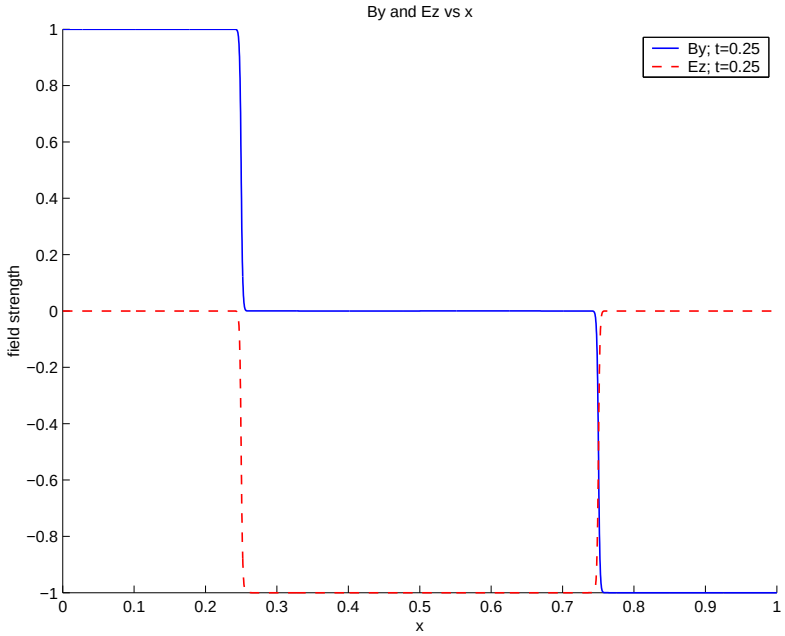

Figure 4.15: B_y and E_z in the non-neutral gas dynamic limit. Since there is no coupling between the fluid and the electromagnetic field, the shock in B_y propagates out at the speed of light. The electromagnetic wave is propagating at the right speed because it has traveled across $\frac{1}{4}$ of the domain in $0.25\tau_c$.

4.3.3 Solutions between the gas dynamic and MHD limits

The two-fluid equations can be used to solve the Brio and Wu [7] shock problem at different Debye lengths and Larmor radii. In the following the Larmor radii will be presented since the Debye lengths are dependent on the Larmor radii in these particular simulations. The MHD solution differs substantially from the two-fluid solution for larger Larmor radii. When the Debye length and Larmor radius are relatively large, terms that are neglected in the MHD approximation become important. In particular, the Hall current and the ion current become important as well as the rate of change of current. In Figures 4.16-4.22, physics beyond MHD is apparent.

Scaling

The non-dimensionalizations in Section 2.3.1 suggests a simple scaling relation. In this problem the ratio $\frac{\lambda_d}{r_{g\,i}}$ gives the ratio of Alfven speed to the speed of light and the ratio is kept constant in these problems. However $L = \frac{x_0}{\lambda_d}\frac{r_{g\,i}}{\lambda_d}$ and $C = \frac{x_0}{r_{g\,i}}$ so if λ_d and $r_{g\,i}$ are kept constant and x_0 is allowed to change, the coupling of the equations can be altered. This means that increasing λ_d and $r_{g\,i}$ is equivalent to decreasing the time and space scales while decreasing λ_d and $r_{g\,i}$ is equivalent increasing the time and space scales. Consequently the problems that follow are exactly the same problem with different time and space scales. In particular, if $r_{g\,i} = 0.1$ in one simulation at a length scale of 1 and a time scale of $10\tau_c$, this is equivalent to looking at the simulation $r_{g\,i} = 1$ at a length scale of 10 and a time scale of $100\tau_c$; $\frac{\lambda_d}{x_0}$ and $\frac{r_{g\,i}}{x_0}$ are scaling parameters.

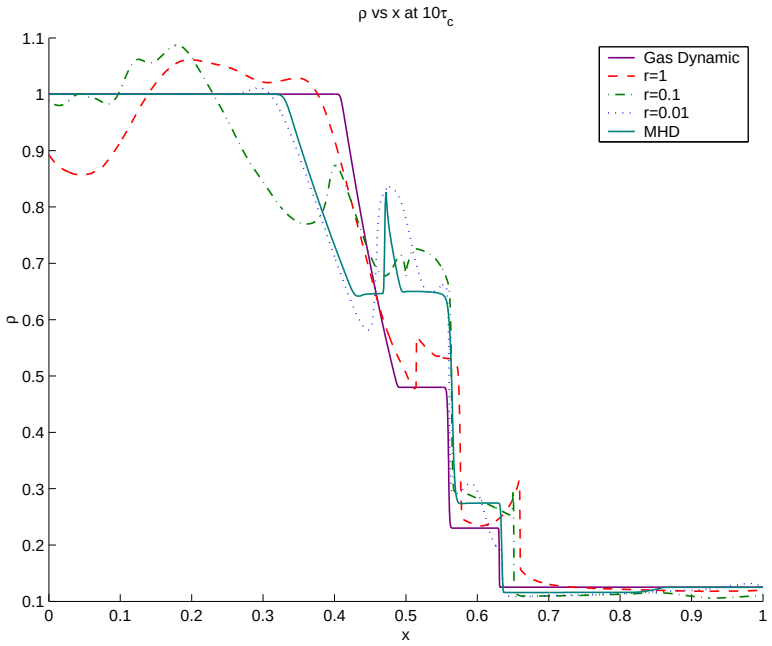

Figure 4.16: Density profile for several values of $r_{g\,i}$. The complexity of the shock problem is evident when the Larmor radius is varied. For example, $r_{g\,i}$=0.1 is not bounded by $r_{g\,i}$=0.01 and $r_{g\,i}$=1 as one might expect.

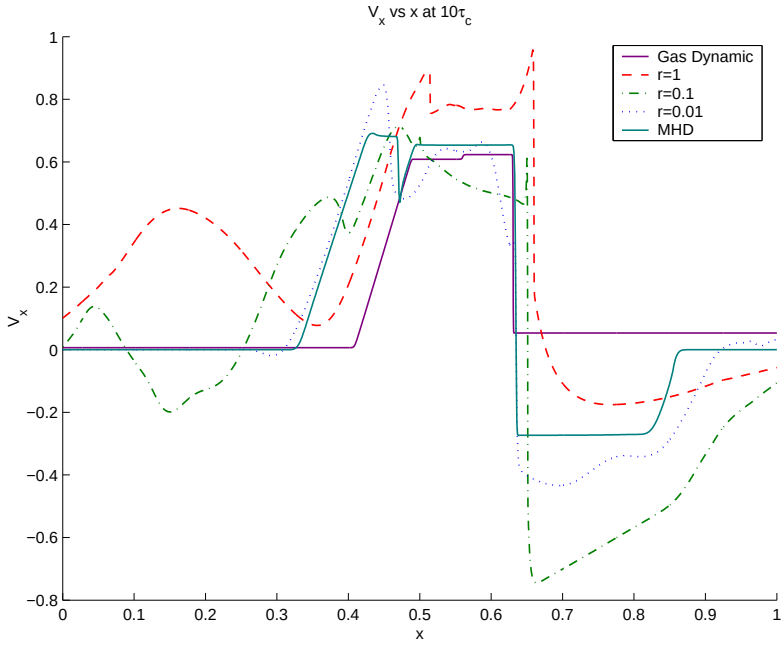

Figure 4.17: V_x profile for several values of r_{gi}. The large bumps outside of the shock are waves quickly propagating out of the domain. If the scaling relation is considered then it should be noticed that as r_{gi} is decreased there are fewer of these waves. There are fewer waves because the fast waves have propagated out of the domain in the snapshot given by the smaller r_{gi}. Recall that decreasing r_{gi} by a factor of 100 is equivalent to leaving r_{gi} the same and increasing the spatial scale of the grid by 100 and increasing the time scale to $1000\tau_c$. If a fast wave is generated sometime after the shock is created it will appear in the plots at large r_{gi}, but not in the plots for small r_{gi}.

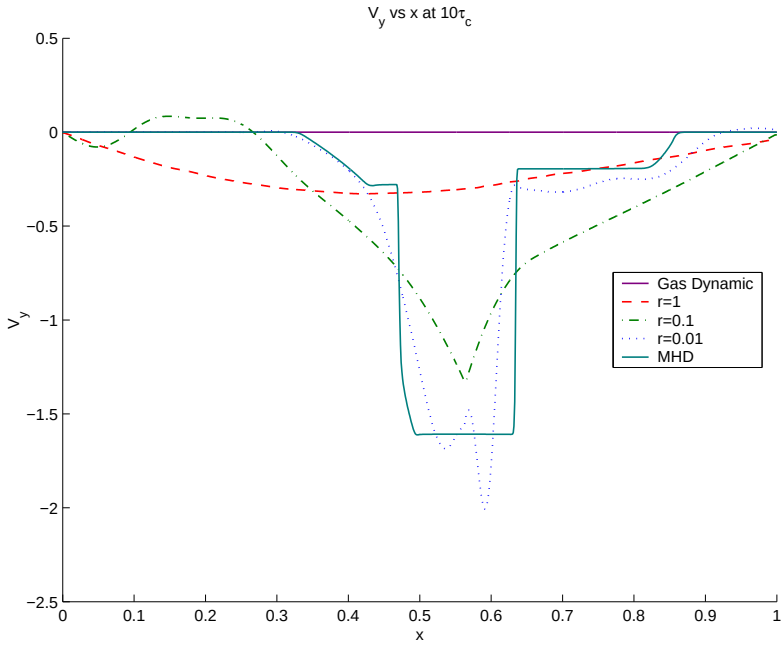

Figure 4.18: V_y profile for several values of r_{gi}. As r_{gi} is decreased, the waves are more confined to the immediate region of the shock. What is really happening, though, is that only the slow waves are being observed because the fast waves have left the domain. When $r_{gi} = 0.1$ more fast waves are observed because they are generated early in the shock formation and haven't left the domain.

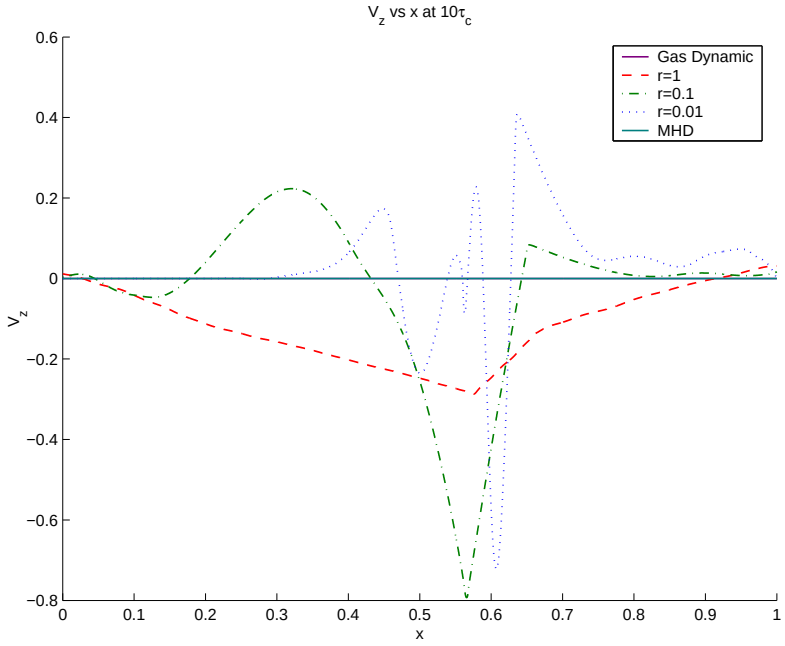

Figure 4.19: V_z profile for several values of $r_{g\,i}$. V_z supports B_y and spans the length of the B_y shock. For $r_{g\,i} = 1$ the shock hasn't formed yet and the waves seen in $r_{g\,i} = 0.1$ have not yet been created. When the shock forms there should be spikes in V_z to support the shock in B_y.

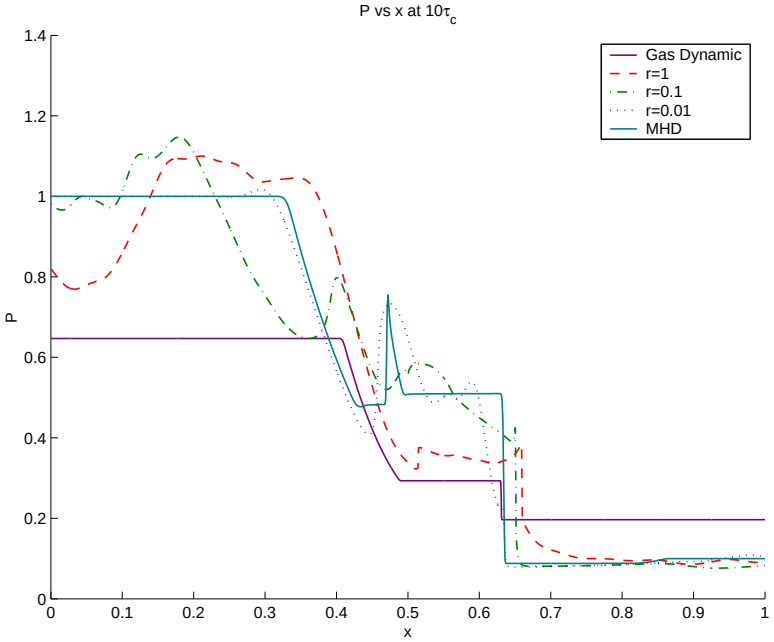

Figure 4.20: Pressure profile for several values of r_{gi}. The gas dynamic pressure drops to roughly half its initially value because the electron shock quickly propagates out of the domain leaving an average background electron pressure. Even with a Larmor radius on the scale of the plasma size, $r_{gi} = 1$, the effects of the magnetic field produce a very different solution from the non-neutral gas dynamic shock.

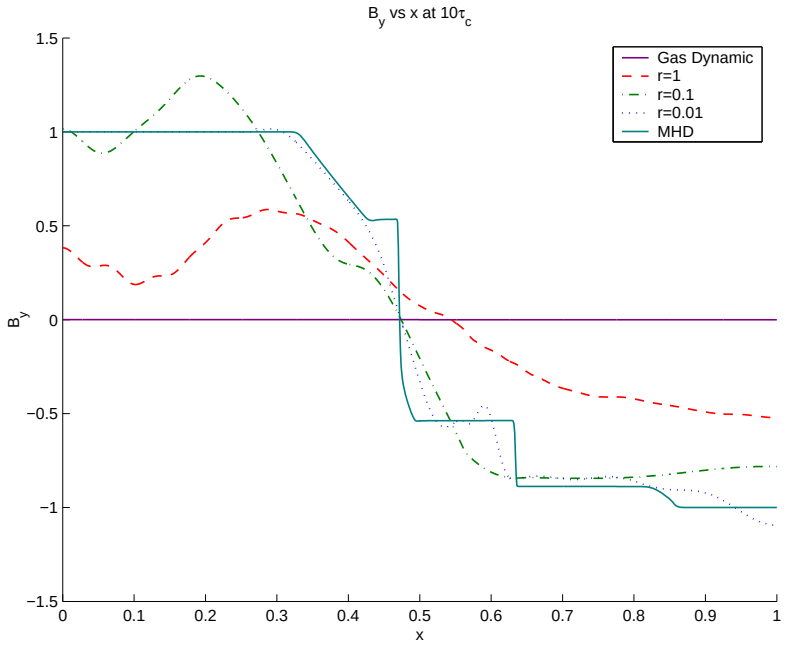

Figure 4.21: B_y profile for several values of r_{gi}. The smaller the Larmor radius the more the magnetic field is frozen into the fluid. It is clear that the propagation speed of the magnetic shocks is related to the Larmor radius. However, early in time the shock should propagate like an electromagnetic wave at near the speed of light because the currents that are generated are small. Eventually the low frequency magnetic fields will generate significant currents which will slow down the low frequency electromagnetic waves so that at a much later time, the same shock appears to have slowed down. The high frequency components leave the domain while the very low frequency components freeze into the fluid.

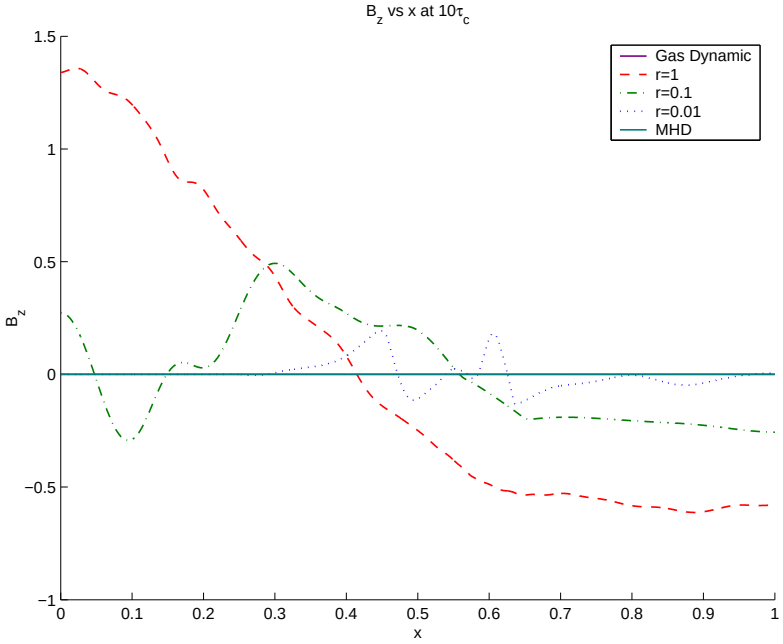

Figure 4.22: B_z profile for several values of $r_{g\,i}$. In both the MHD and non-neutral gas dynamic limits, the B_z drops to zero. When $r_{g\,i}$=1, the magnetic field is frozen into the fluid slightly and has not had time to propagate out. The magnitude of B_z decreases as $r_{g\,i}$ decreases, just as the MHD limit predicts.

4.3.4 Convergence

Many of the previous simulations have been run at several grid resolutions to look at convergence of the solutions. As the MHD limit is approached the problem becomes stiffer and convergence to the correct solution becomes more difficult. In the MHD limit a shock wave in B_y must be supported by a delta function in J_z. Similarly, a shock in P must be supported by a delta function in E_x according to the description of a plasma shock as an electron shock and an ion shock separated by a small distance. Similar statements can be made about other plasma variables where a shock in one variable requires a delta function in another variable to support the shock. Delta functions cannot be resolved numerically so at these points, no matter how fine the grid resolution is made, the error would remain infinitely large. Fortunately with finite λ_d and $r_{g\,i}$ none of the shocks that occur in the two-fluid system are true discontinuities and so none of the delta functions which would be associated with these shocks are true delta functions, the are merely large spikes in the data. These spikes can be resolved numerically. From now on the word "delta function", or "spike", is used to mean a finite spike in the solution which is associated with a shock in some other variable.

In Figures 4.23-4.32, it is observed that the solution is well resolved in smooth regions. However, all the profiles have delta functions where the solution changes substantially for each grid refinement. Ultimately it is expected that the solutions near these spikes will eventually be resolved, but at a substantially higher grid resolution than the rest of the solution. It is interesting to note that several of the profiles corresponding to Figures 4.23, 4.24, 4.27, 4.28, 4.32, are well resolved over the majority of the solution with 1000 grid cells. On the other hand the profiles corresponding to Figures 4.26, 4.29, 4.30, 4.31, exhibit substantial differences between 4000 grid cells and 2000 grid cells. The characteristic of the later plots is that all of them have several delta functions which dominate the profile. It should be noted that the Debye length is not resolved in these simulations, Figures 4.23-4.32. This seems to suggest that it is not necessary to resolve the Debye length except in the vicinity of shocks or steep gradients.

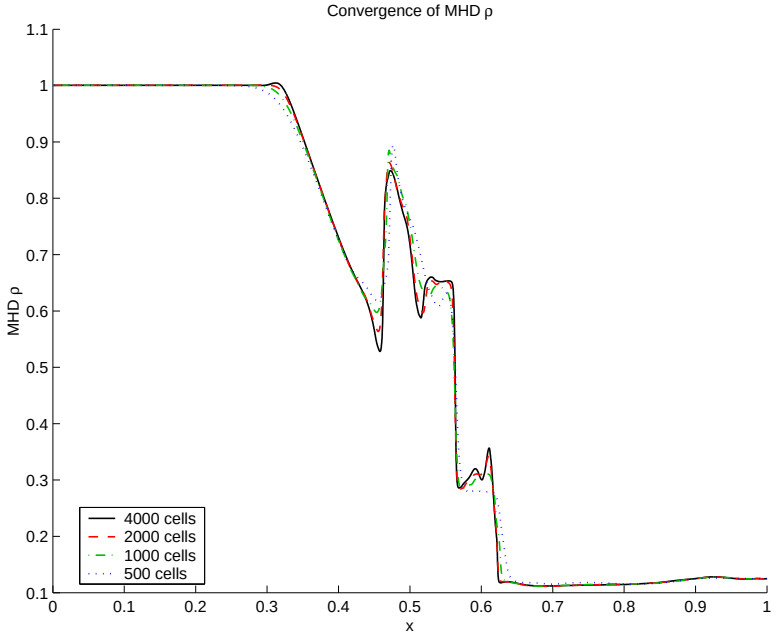

Figure 4.23: Convergence of MHD ρ as the grid is refined. The solution is well resolved except at sharp corners.

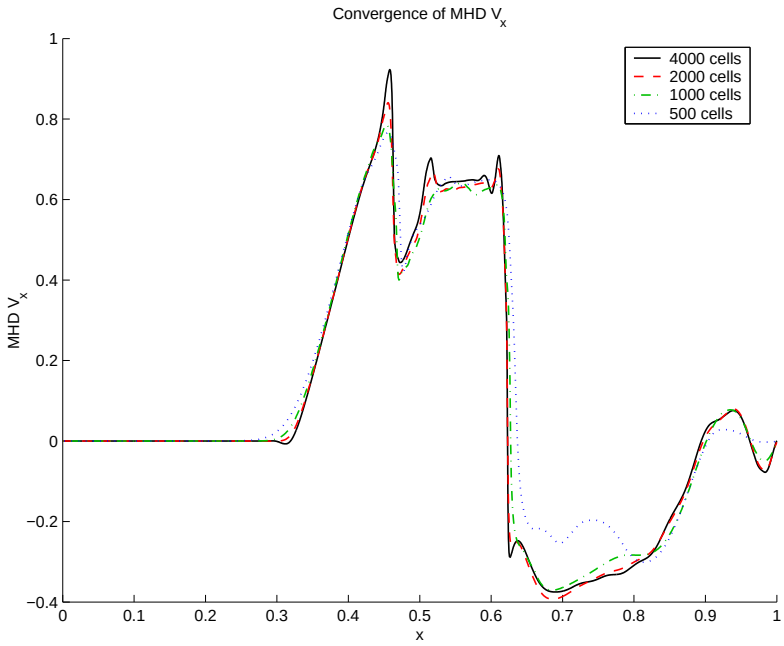

Figure 4.24: Convergence of MHD V_x as the grid is refined. The solution is well resolved everywhere except for in the vicinity of the spikes. It is unclear if these small spikes are numerical or physical.

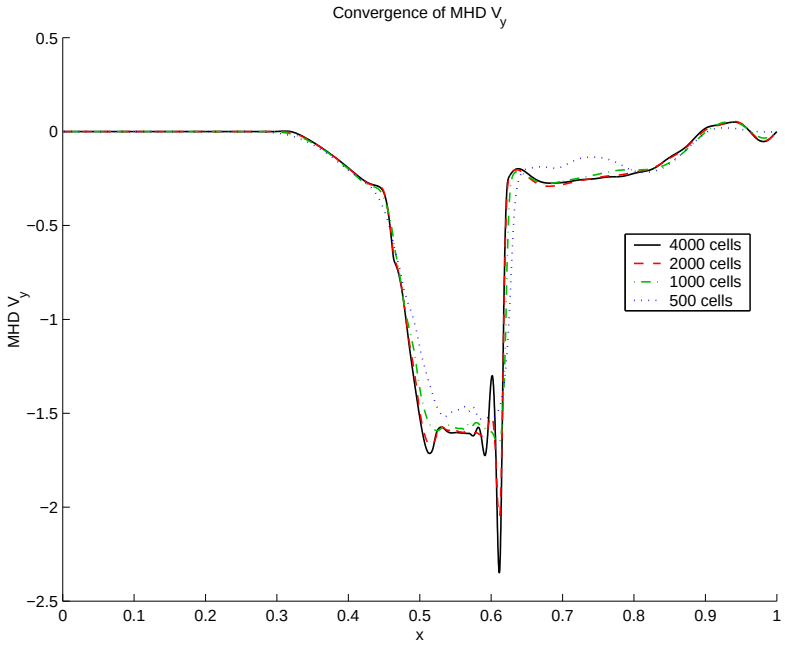

Figure 4.25: Convergence of MHD V_y as the grid is refined. Although the homogeneous solution is TVD and should therefore not produce any oscillations, the existence of the source terms and the delta functions at the shocks may be introducing extra oscillations behind the delta function which are non-physical.

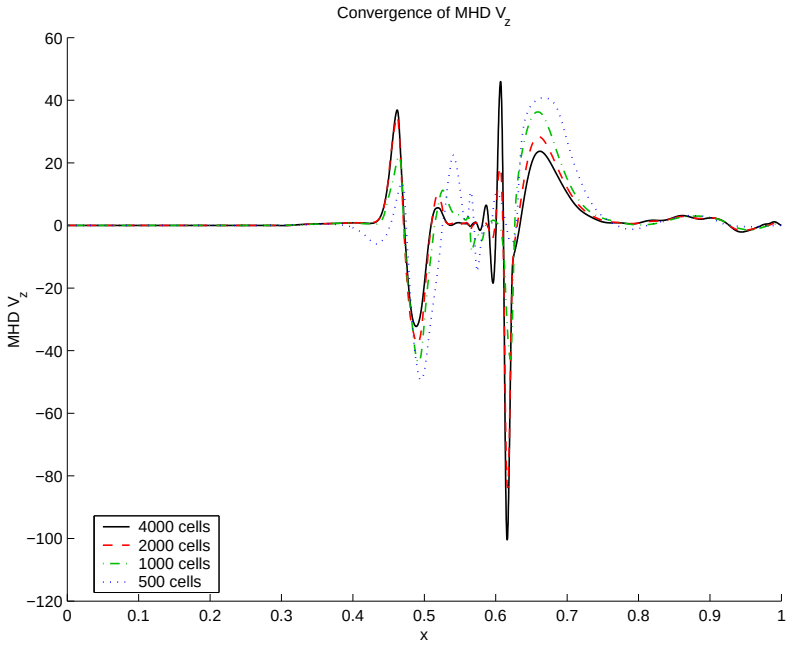

Figure 4.26: Convergence of MHD V_z as the grid is refined. The large delta function indicates a region of the fluid that is traveling at almost the speed of light. It may be more appropriate to include relativistic electrons in these simulations. The finer the grid gets, the larger velocities in the spikes will get until the solution is well resolved.

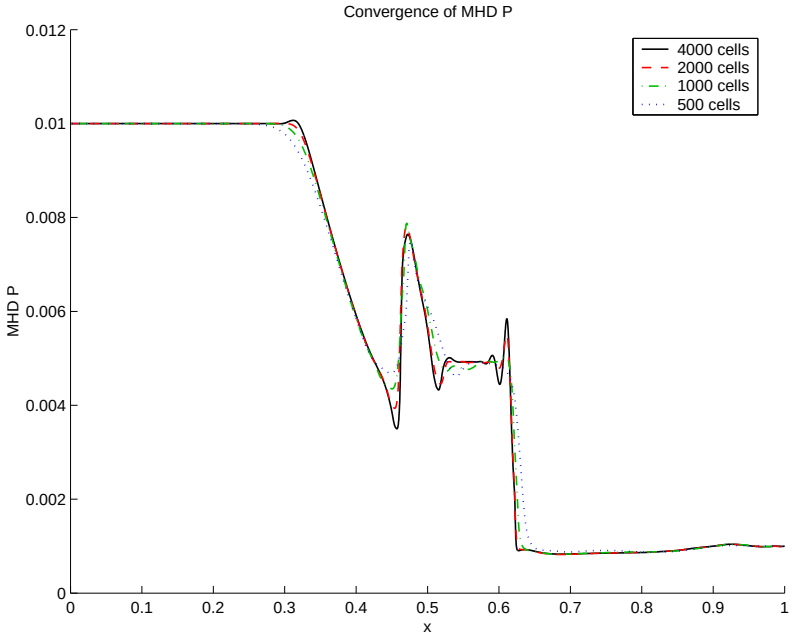

Figure 4.27: Convergence of MHD P as the grid is refined. Several spikes occur in this pressure profile, some of which may be numerical.

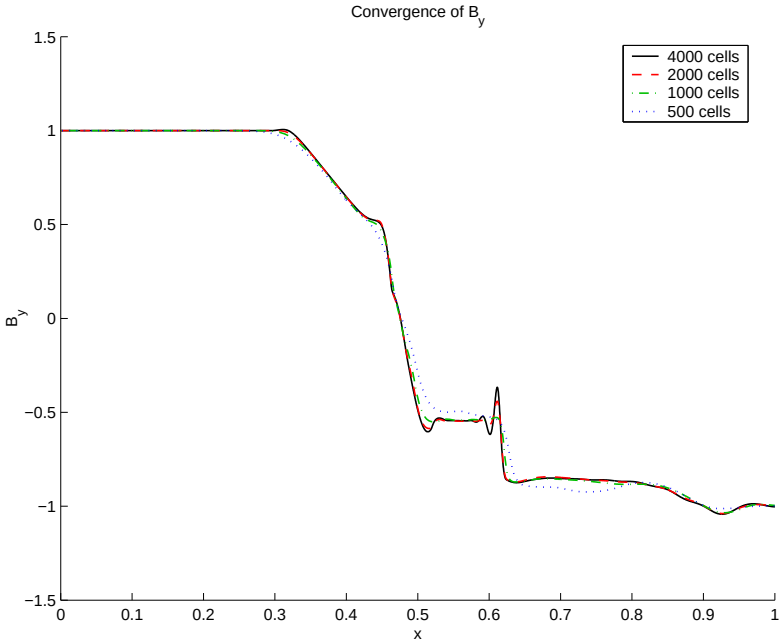

Figure 4.28: Convergence of B_y as the grid is refined. 500 cells resolves this component of the B field well.

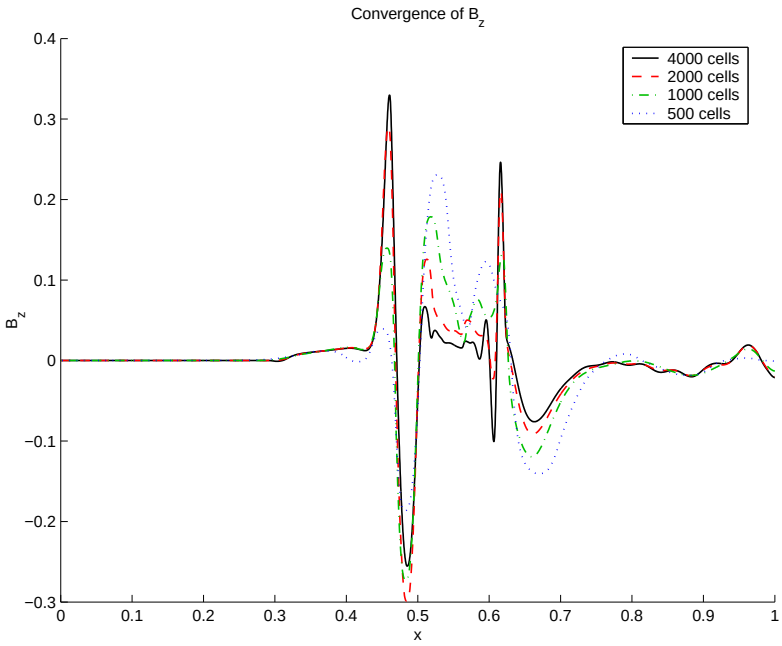

Figure 4.29: Convergence of B_z as the grid is refined. B_z is not well resolved even at 2000 cells. The presense of several delta functions may contribute to the fact that this component of the B field changes so much with grid resolution.

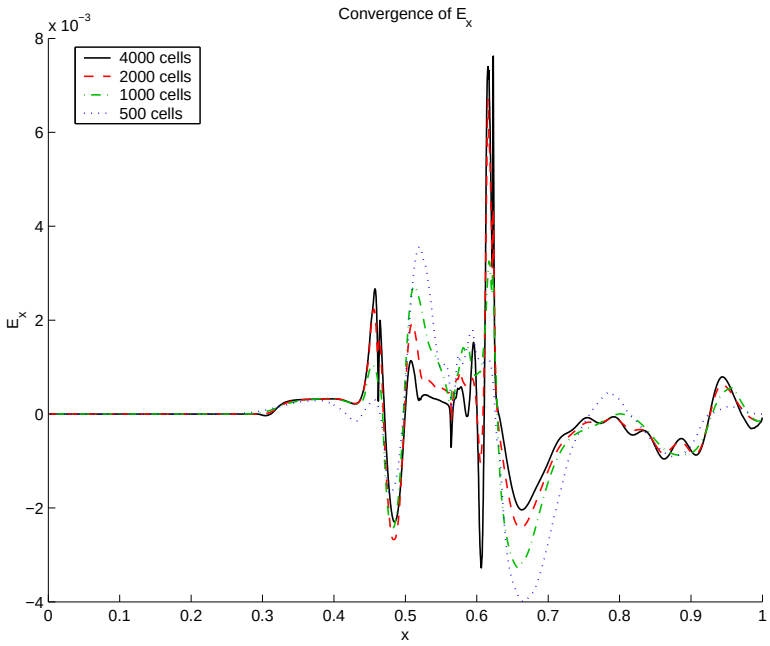

Figure 4.30: Convergence of E_x as the grid is refined. In this profile a spike at 2000 cells breaks into two spikes at 4000 cells indicating that grid resolution is not high enough to resolve the structure. At 4000 cells the Debye length is not resolved. The large spike in E_x is expected because it corresponds to the shock in number density. A finite separation between the electron shock and the ion shock produces this shock in E_x.

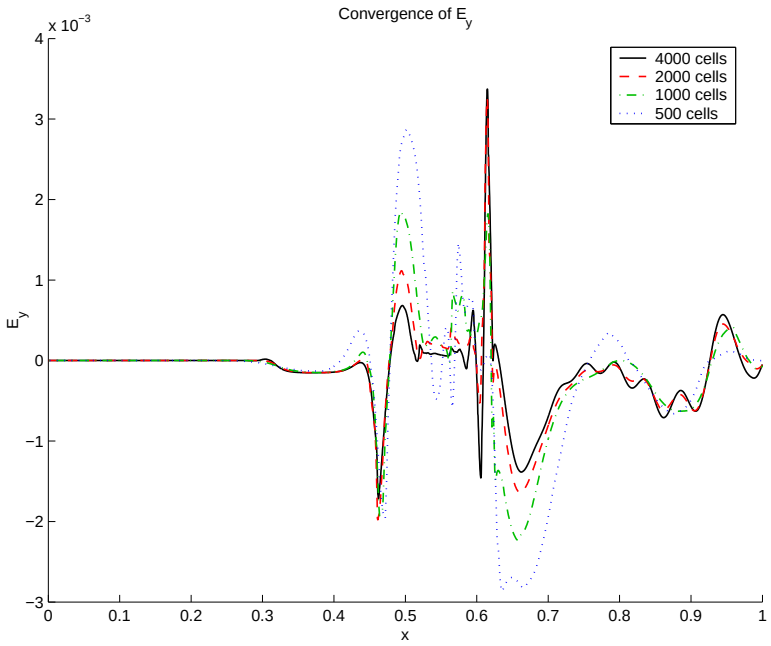

Figure 4.31: Convergence of E_y as the grid is refined. Large changes in E_y are observed as the grid is refined. At a resolution of 4000 cells short wavelength oscillations appear on the right hand side of the solution.

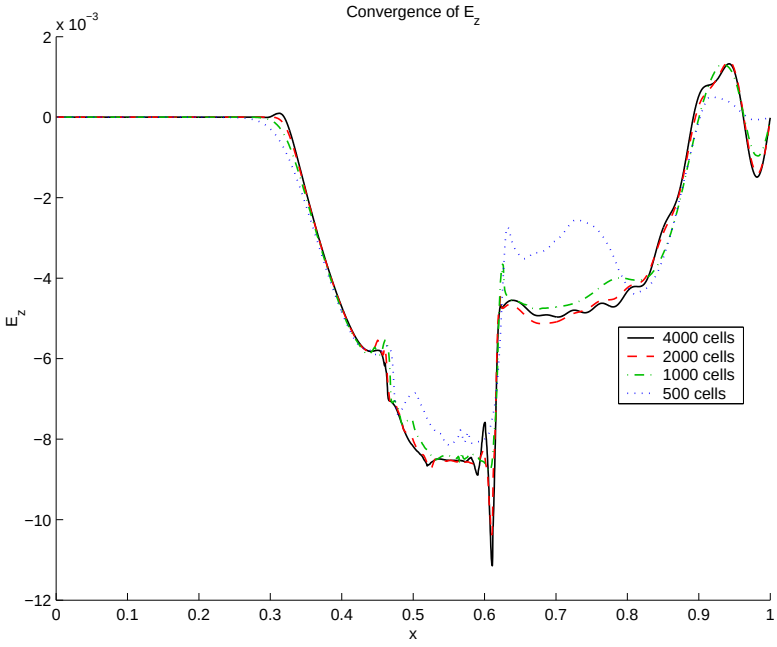

Figure 4.32: Convergence of E_z as the grid is refined. E_z is fairly well resolved at a grid resolution of 1000 cells.

4.3.5 Fast waves

The following simulations, Figures 4.33, 4.34, 4.35, are the same as those in section 4.3.3, except that the simulations are plotted at $0.25\tau_c$. Most of the waves that appear here are fast waves which quickly propagate out of the domain. One common theme is that as the Larmor radius is decreased the high frequency waves travel slower and slower. In ideal MHD the magnetic field is frozen in to the fluid, which is to say that the magnetic field does not move unless the fluid moves as well, therefore the magnetic field should freeze to the bulk fluid shock. Figure 4.34 shows the magnetic field freezing into the fluid as the Larmor radius is reduced. At $r_{g\,i}$=10 the B_y shock moves at about the speed of light, whereas at $r_{g\,i}$=0.1 the wave is much slower. Notice also that the low frequency waves travel slower than the high frequency waves. The MHD equations assume the fast waves (high frequency) are insignificant and propagate out of the domain quickly which is a valid assumption as demonstrated by Figure 4.34.

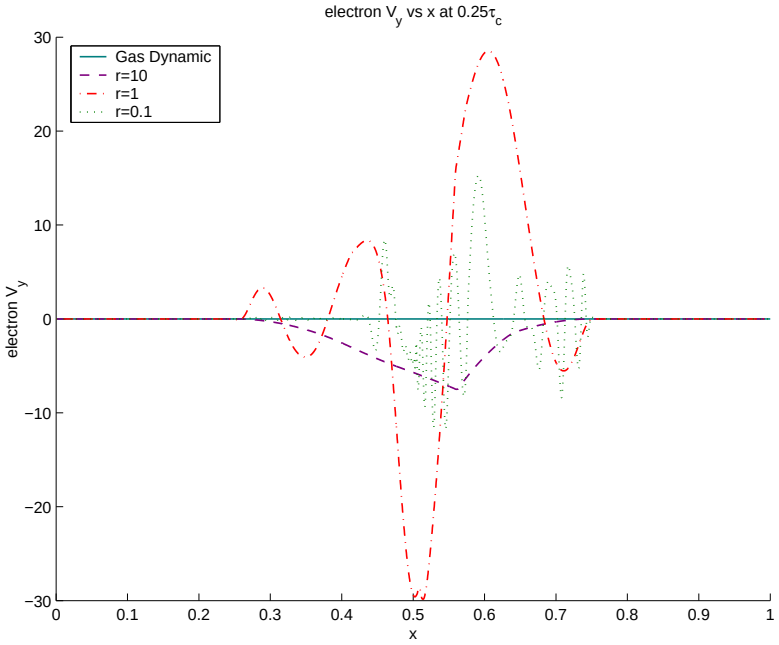

Figure 4.33: V_y profile for various $r_{g\,i}$. As the coupling between the electromagnetic field and the fluid increases, the shock in B_y is supported by higher and higher frequency components of the electron current. The electron current becomes several current spikes in the MHD limit.

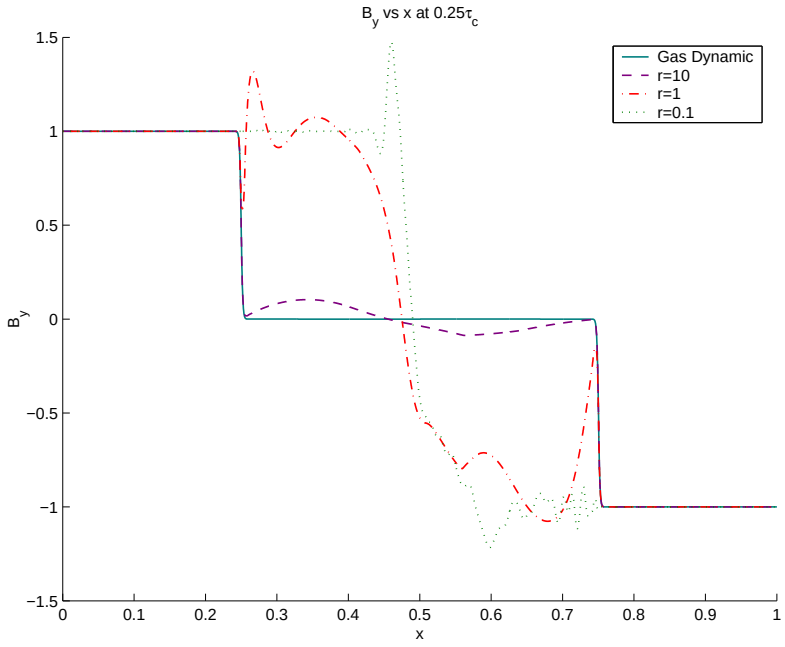

Figure 4.34: B_y profile for various $r_{g\,i}$. Notice that the high frequency waves travel faster than the low frequency waves. Furthermore, on the high density side of the shock the electromagnetic waves slow down where $r_{g\,i}$=0.1 and form a spike right near the shock. This looks like numerical dispersion, but it is actually a result of electromagnetic wave dispersion in a plasma.

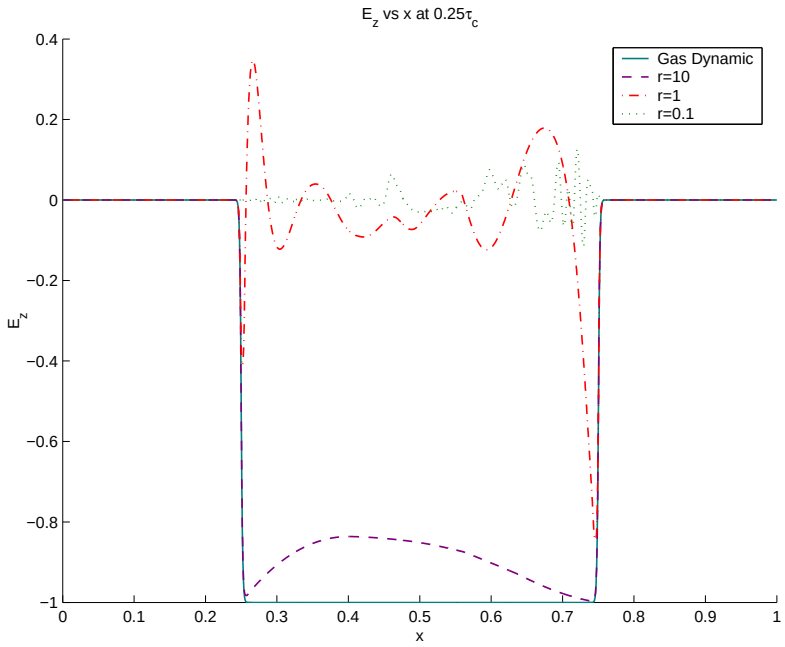

Figure 4.35: B_z profile for various $r_{g\,i}$. Propagating electromagnetic waves from the B_y shock should produce an E_z. If B_y was supported entirely by E_z, E_z would have the same magnitude as B_y. It is clear that because the magnitude of E_z is decreasing with respect to B_y as the Larmor radius is decreased, more and more of B_y is being supported by J_z. In the MHD limit, the effect of the displacement current disappears altogether, which is consistent with these simulations.

4.4 Two-Fluid Plasma Waves

The two-fluid dispersion relationships can be observed in the electromagnetic shock problem. Using the result from the electromagnetic shock with a $r_{g\,i} = 0.1$, the results are Fourier decomposed for all space for the first $5\tau_c$ and then the log of the magnitude of the resulting matrix are taken. Red indicates a region of high amplitude whereas blue represents a region of small amplitude waves. The R-mode, L-mode, whistler and electron plasma waves are clearly observed as is demonstrated in Figures 4.36-4.38.

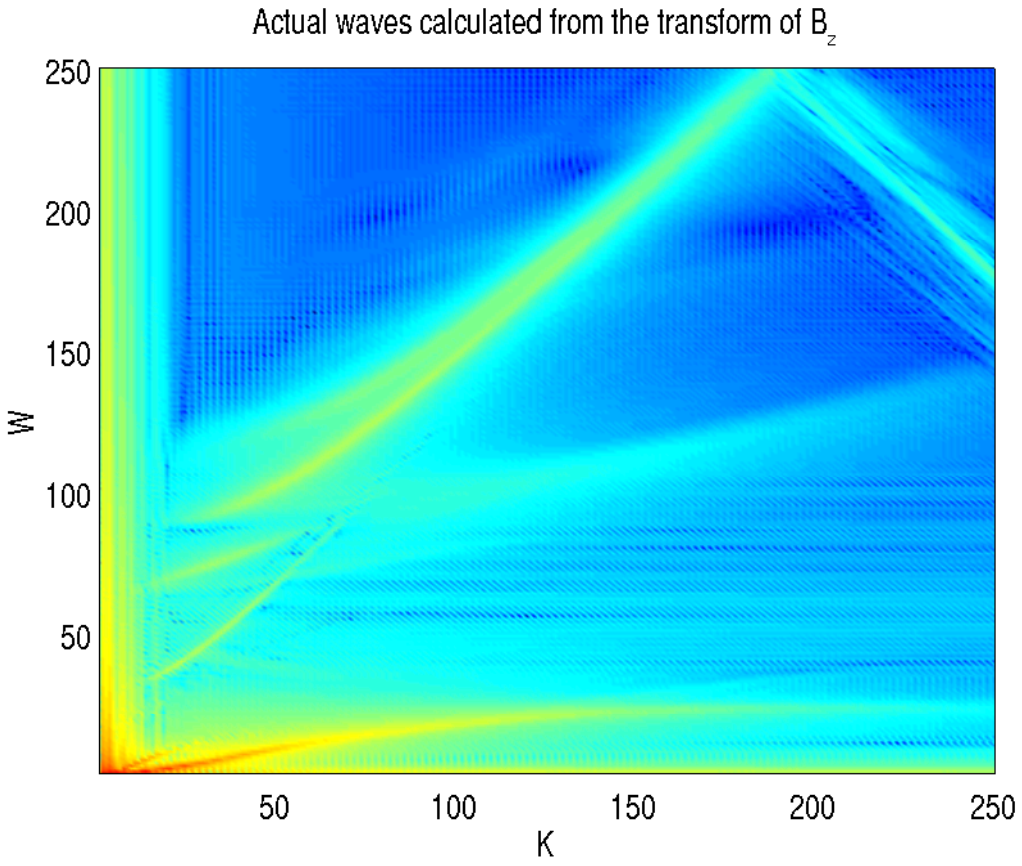

Figure 4.36: Calculated dispersion diagram. The two-fluid Riemann problem for r=0.1 was Fourier decomposed for the first $5\tau_c$ and over all space to create this dispersion relationship. W is a scaled frequency and K is a scaled wave number for waves in the plasma. The graph clearly indicates the presense of several dispersion relationships. In the following it will be shown that these are actually two-fluid plasma waves and not a result of numerical dispersion.

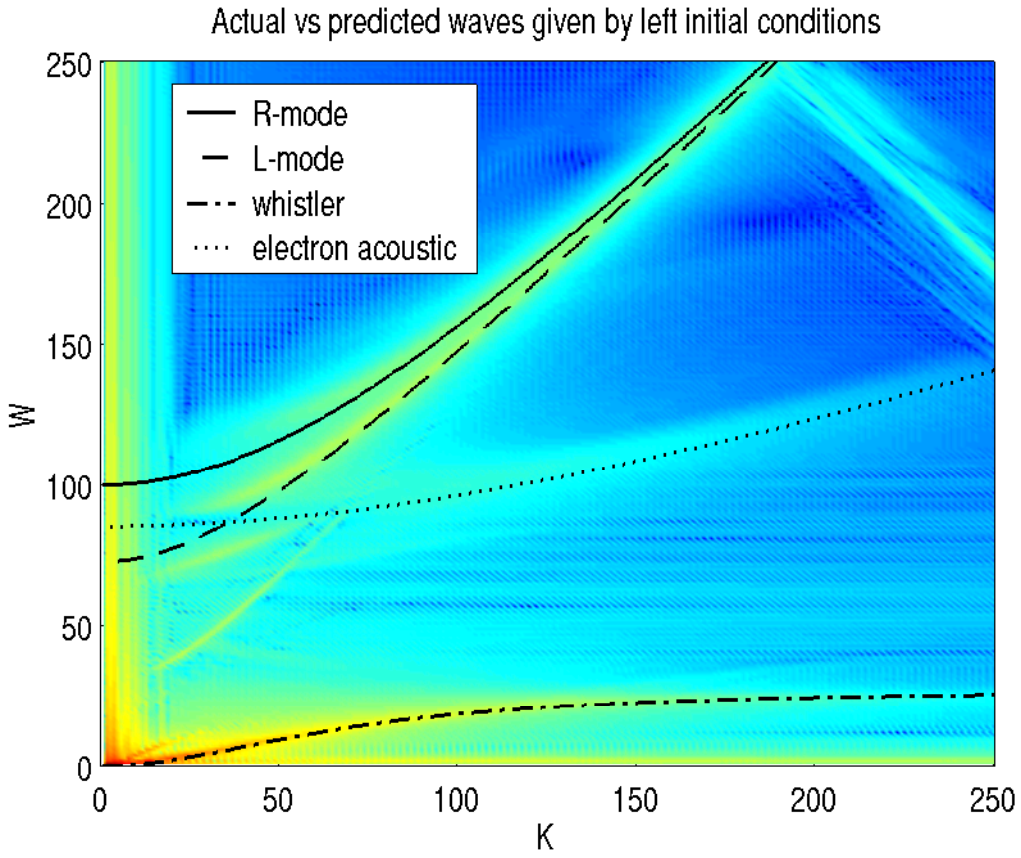

Figure 4.37: Analytic verses calculated dispersion diagram using the initial conditions on the left half of the shock for the analytic solution. The R-mode, L-mode, whistler, and electron acoustic waves match the solution calculated by the two-fluid algorithm. The dispersion relations given in the previous section apply for high frequency therefore it is reasonable that the waves should differ slightly from the predicted values on the low wave number side of the plot.

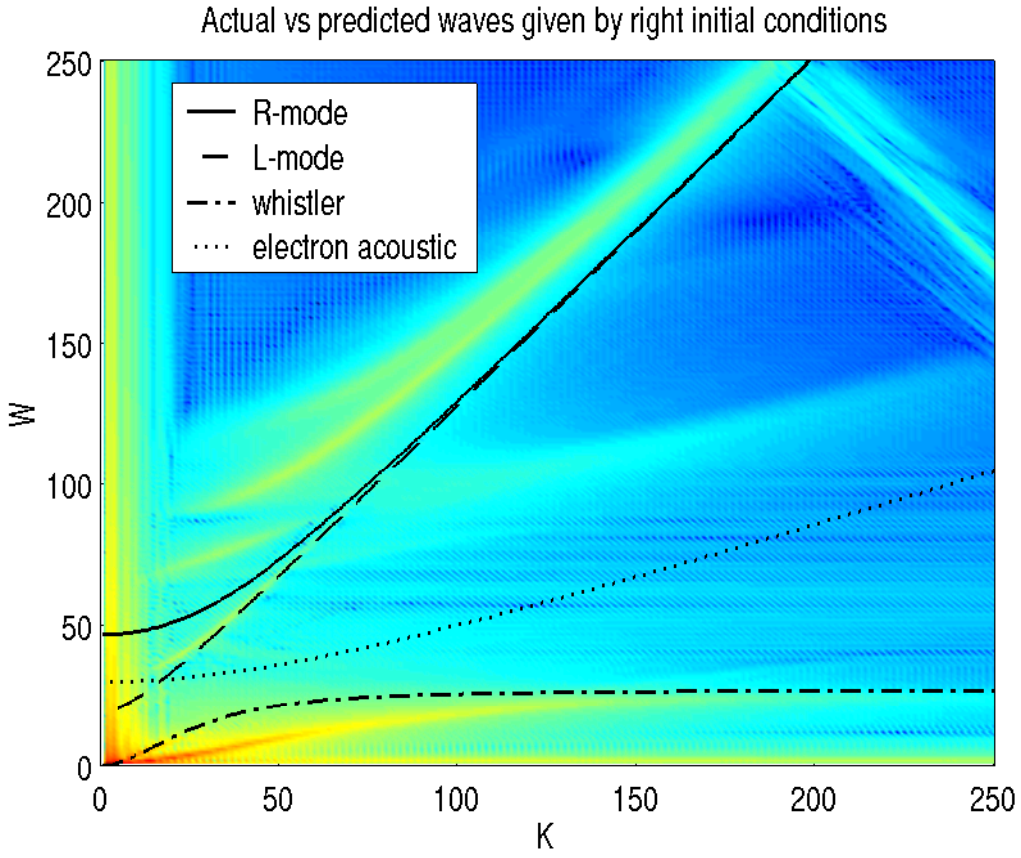

Figure 4.38: Analytic verses calculated dispersion diagram using the initial conditions on the right half of the shock for the analytic solution. On the right side of the shock, only the L-mode wave and whistler wave seem to match the the dispersion graph. In fact, from the very beginning the L-mode wave is traveling at nearly the speed of light. It is assumed that the majority of waves on the right side of the shock are of such low frequency that the high frequency components do not show up in the dispersion diagram.

4.5 Electrostatic Shock

The electromagnetic shock can be made into an electrostatic shock by setting the magnetic field to zero. In this case there should be no electromagnetic waves. In the following the number density for both the electrons and ions is plotted. Notice that in all cases the quasi-neutrality condition is maintained except in the vicinity of shocks where the electron and ion number densities differ substantially. The non-dimensionalization in Section 2.3.2, is used in these simulations. It should be noted that the scaling given in Section 4.3.3, applies and the following simulations can be considered the same problem plotted at different times and with different spatial scales. In this regard Figure 4.39 can be considered a plot of the formation of the shock early in time and Figure 4.42 can be considered a plot of the shock at a spatial x scale 1000 time greater at a time 1000 times later. Figures 4.40 and 4.41 give solutions at intermediate Debye length. It is unclear if the spikes are physical or are a result of numerical errors.

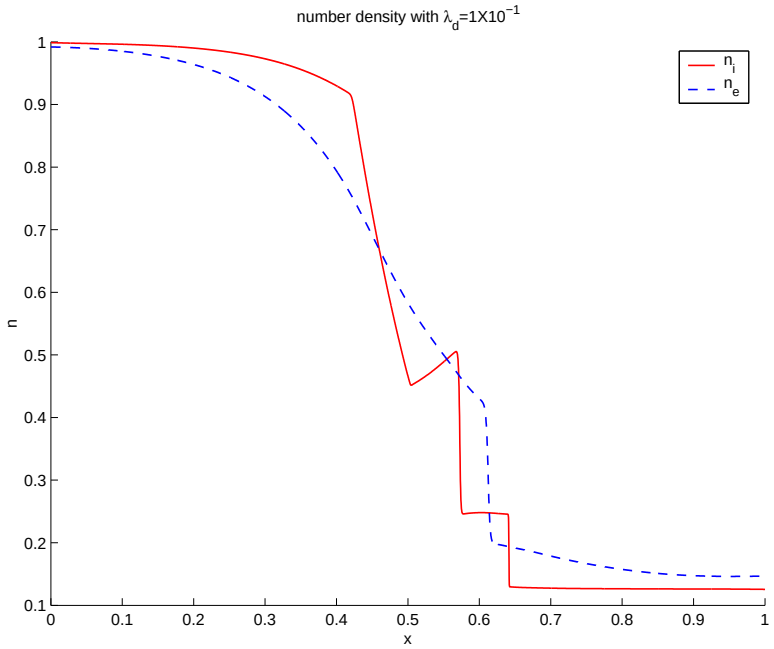

Figure 4.39: Electrostatic shock with $\lambda_d = 0.1$. The electron fluid separates from the ion fluid in all regions except those far from the shock. Electric fields should be shielded out in roughly $\frac{1}{10}$ the domain in steady state.

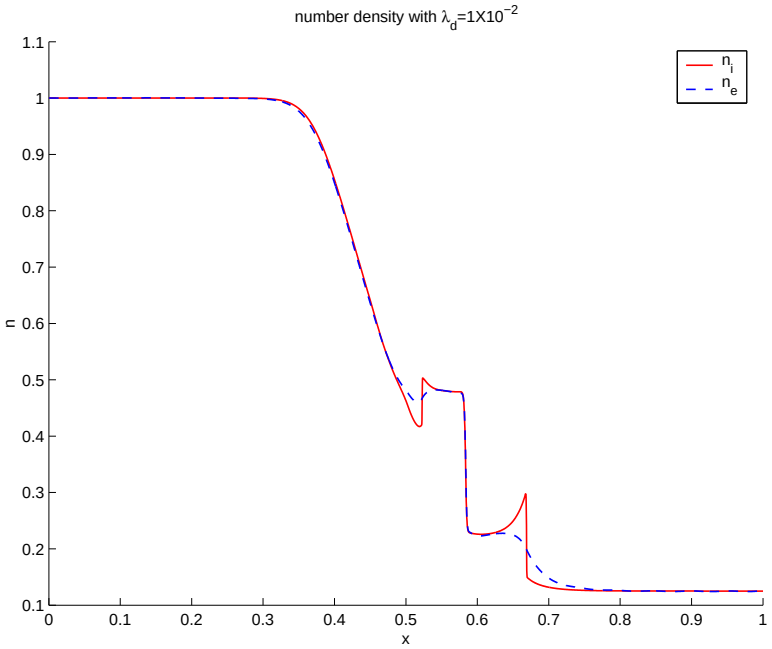

Figure 4.40: Electrostatic shock with $\lambda_d = 0.01$. The electron fluid is bound tighter to the ion fluid and the first signs are visible that spikes in the ion fluid are appearing. The ions in the leading edge ion shock appear to be accelerating to match the electron shock speed. The ion number density builds up on the front of the leading edge shock which in turn allows more electrons to propagate forward. Through this process the electron fluid accelerates the ion fluid until an equilibrium is reached.

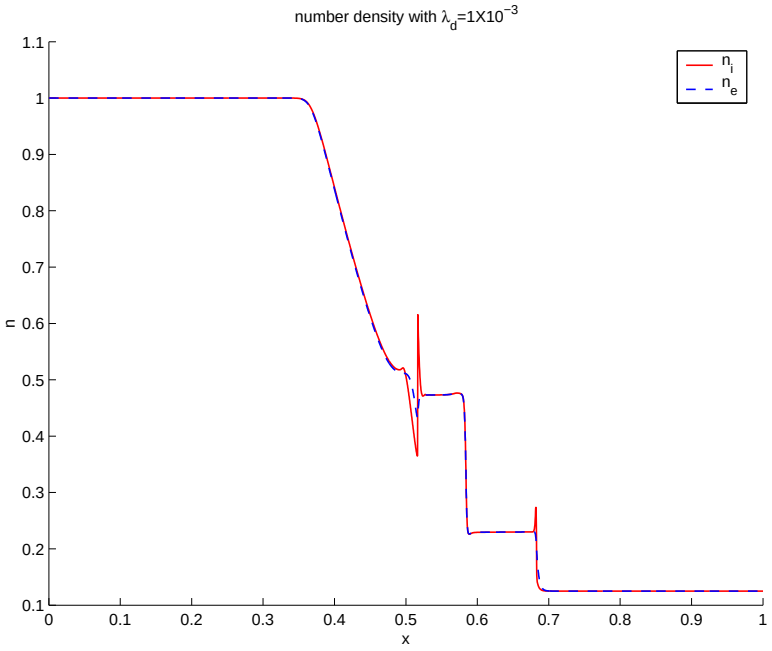

Figure 4.41: Electrostatic shock with $\lambda_d = 0.001$. Three spikes are fully developed near the shocks of the ion fluid. The electron fluid maintains a smooth profile. The electrons do not follow the ion spikes so if the spikes are physical the electron momentum flux across the shock must be balancing with the force from the electric field to keep the electrons from moving into the spikes. It should also be noted that the electron plasma waves have already propagated out of the domain leaving only the lower frequency waves.

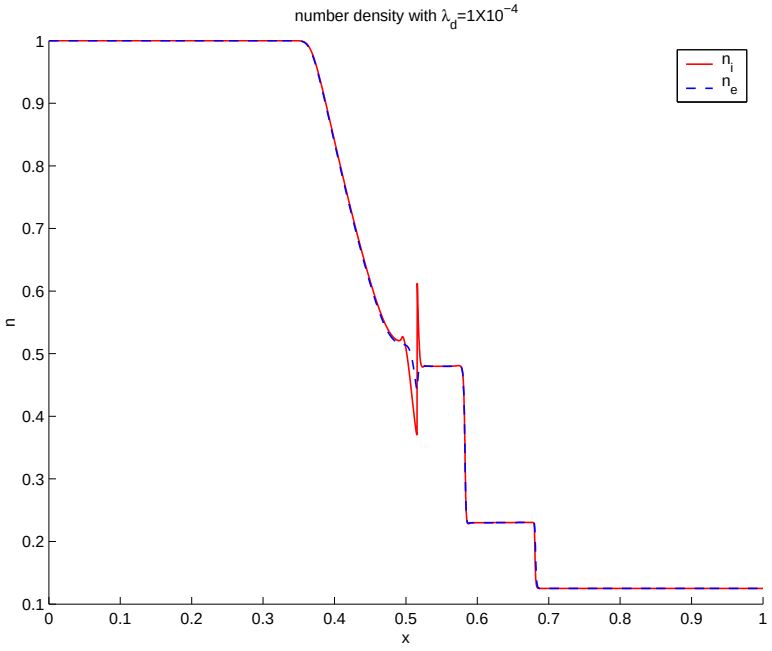

Figure 4.42: Electrostatic shock with $\lambda_d = 0.0001$. One spike on the ion fluid is smoothed out and the shock speed of the bulk fluid has increased. The electrons are essentially stuck to the ions and the pressures of the two fluids are coupled through the electric field. The acoustic speed of the ion-electron fluid can be calculated by adding the electron and ion pressures. This acoustic speed is greater than the ion acoustic speed so the speed of the ion-electron shock is faster than the speed of the ion shock alone. In this plot the ion shock has finally reached and equilibrium with the electron shock. The spike on the leading edge shock is gone, this may simply be because the grid resolution is not fine enough to resolve the spike at this scale.

Chapter 5

CONCLUSION AND FUTURE WORK

A numerical algorithm for solving the two-fluid plasma system of equations has been developed. The homogeneous parts are solved using a Roe approximate Riemann solver and the source terms are updated either implicitly or explicitly. A modified potential formulation has been explored to satisfy Poisson's equation, although its use is limited to problems where the system is not stiff and is therefore of little interest to us. It has been found that the relevant time scales of each simulation are the electron plasma frequency or that determined by the CFL condition applied to the speed of light. In the presense of shocks the relevant spatial scales appear to be on the order of the Debye length (although this remains to be verified). In smooth regions the solution is accurately resolved with some large multiple of the Debye length. The algorithm is shown to work well in regimes with both strong and weak coupling and approaches the limits leading to the MHD solution and the non-neutral gas dynamic solution with free electromagnetic fields. This suggests that the solutions bounded by these two limits have also been solved correctly. The electrostatic shock was solved for several Debye lengths. Finally it has been shown that the algorithm captures a variety of waves predicted by the dispersion relations obtained from linearizing the two-fluid equations.

Solving this system of equations is computationally intensive and future work, and in particular, extension to three dimensions, will have to keep this in mind. Stiff, high-resolution problems in one dimension typically take several days to run on a single 433MHz DEC Alpha. In three dimensions, stiff, high resolution runs will require an efficiently written algorithm and parallel computation. Stiffness due to the plasma frequency could be alleviated with a more efficient algorithm. Some work needs to be done to determine how much of the oscillations produced by spikes are real and how much is numerical. The two-fluid system presents new problems because it is necessary to resolve these spikes. Typical fusion plas-

mas are characterized by Debye lengths $\frac{1}{10}$ to $\frac{1}{100}$ those obtained in the stiffest simulations described in this thesis. With the help of parallel computers simulations of this type are obtainable using the technique described. Satisfying the magnetic flux condition (2.8) and Poisson's equation (2.7) will be more important in three-dimensions so that errors in the electric and magnetic fields do not grow out of hand.

BIBLIOGRAPHY

[1] Necdet Aslan. Two-dimensional solutions of mhd equations with an adapted roe method. *International Journal for Numerical Methods in Fluids*, 23:1211–1222, 1996.

[2] Necdet Aslan and Terry Kammash. Developing numerical fluxes with new sonic fix for mhd equations. *Journal Of Computational Physics*, 133:43–55, 1997.

[3] T.J Barth and H. Deconinck. *High-Order Methods for Computational Physics*. Springer, 1999.

[4] D. Biskamp, E. Schwarz, and J.F. Drake. Two-fluid theory of collisionless magnetic reconnection. *Physics of Plasmas*, pages 1002–1009, 1997.

[5] T.K. Bose. A cfd study of hypersonic weakly-ionized argon plasma flow. In *35th AIAA Thermophysics Conference*, 2001.

[6] J.A. Breslau and S.C. Jardin. A parallel algorithm for global magnetic reconnection studies. *Computer Physics Communications*, 151:8–24, 2003.

[7] M. Brio and C. C. Wu. An upwind differencing scheme for the equations of ideal magnetohydrodynamics. *Journal Of Computational Physics*, 75:400–422, 1988.

[8] G. Caldo and E. Choueiri. An mpd code with anomalous transport. In *22nd International Electric Propulsion Conference*, 1991.

[9] Francis Chen. *Introduction to Plasma Physics and Controlled Fusion*. Plenum Press, 1984.

[10] Arpad Csik, Hans De Sterk, Bart van der Holst, Herman Deconinck, and Stefaan Poedts. Parallel residual distribution solver for ideal 3d magnetohydrodynamic equations: Application to flows in space physics. In *15th AIAA Computational Fluid Dynamics Conference*, 2001.

[11] Jeffrey P. Freidberg. *Ideal Magnetohydrodynamics.* Plenum Press, 1987.

[12] R. J. Goldston and P. H. Rutherford. *Introduction to Plasma Physics.* Institute of Physics Publishing, 1995.

[13] Michael Hesse, Joachim Birn, and Masha Kusnetsova. Collisionless magnetic reconnection: Electron processes and transport modeling. *Journal of Geophysical Research*, 106:3721–3735, 2001.

[14] C. Hirsch. *Numerical Computation of Internal and External Flows.* Wiley, 1988.

[15] Ogden S. Jones, Uri Shumlak, and D. Scott Eberhardt. An implicit scheme for nonideal magnetohydrodynamics. *Journal Of Computational Physics*, 130:231–242, 1997.

[16] Dietmar Kroner. *Numerical Schemes for Conservation Laws.* Wiley and Teubner, 1997.

[17] Randall J. LeVeque. Finite difference methods for differential equations. Lecture notes for amath 585-586 at the University of Washington.

[18] Randall J. LeVeque. *Numerical Methods for Conservation Laws.* Birkhauser, 1992.

[19] Randall J. LeVeque. *Finite Volume Methods for Hyperbolic Problems.* Cambridge University Press, 2002.

[20] C. D. Munz, R. Schneider, and U. Vos. A finite-volume method for the maxwell equations in the time domain. *Siam Journal of Scientific Computing*, 22:449–475, 2000.

[21] Bryan V. Oliver and Tom A. Mehlhorn. Nonideal mhd plasma regimes in the study of dynamic pinches. *IEEE transactions on plasma science*, 30(2):517–523, 2002.

[22] A. Otto. Geospace environment modeling (gem) magnetic reconnection challenge: Mhd and hall mhd - constant and current dependent resistivity models. *Journal Of Geophysical Research*, 106:3751–3757, 2001.

[23] P.L. Roe. Approximate riemann solvers, parameter vectors, and difference schemes. *Journal Of Computational Physics*, 135:250–258, 1997.

[24] K. Sankaran, L. Martinelli, S.C Jardin, and E.Y. Choueiri. A flux-limited numerical method for solving the mhd equations to simulate propulsive plasma flows. *International Journal for Numerical Methods in Engineering*, 53:1415–1432, 2001.

[25] R. Schneider and C. D. Munz. The approximation of two-fluid plasma flow with explicit upwind schemes. *International Journal of Numerical Modelling: Electronic Networks, Devices and Fields*, 8:399–416, 1995.

[26] U. Shumlak, R.P. Golingo, B.A. Nelson, and D.J. Den Hartog. Evidence of stabilization in the z-pinch. *Physical Review Letters*, 87(20), 2001.

[27] D.G. Swanson. *Plasma Waves*. Academic Press, 1989.

[28] E.F. Toro. *Riemann Solvers and Numerical Methods for Fluid Dynamics*. Springer, 1999.

[29] Gabor Toth. The divb constraint in shock-capturing magnetohydrodynamics codes. *Journal Of Computational Physics*, 161:605–652, 2000.

[30] Bogdan Udrea. *An Advanced Implicit Solver for MHD*. Ph.d. dissertation, University of Washington, 1999.

[31] R.M. Winglee. Mapping of ionospheric outflows into the magnetosphere for varying imf conditions. *Journal of Atmospheric and Solar-Terrestrial Physics*, 62:527–540, 2000.